THE UNIVERSITY OF READING

Estimation of the Diurnal Variability of Sea Surface Temperatures using Numerical Modelling and the Assimilation of Satellite Observations

Thesis submitted for the degree of

Doctor of Philosophy

School of Mathematics, Meteorology and Physics

Samuel Pimentel

December 6

ABSTRACT

This thesis is concerned with the diurnal cycle of sea surface temperature (SST). The diurnal variability of SSTs are an important feature of the climate system. In order to obtain accurate SST records and reduce errors in satellite derived SST estimates an understanding of the diurnal signals in these observations are essential. Satellite derived SST observations measure the skin and sub-skin layers whereas ocean models typically resolve a 5 metre temperature. An understanding of these di erences are important for assimilation of SST.

In this thesis a one-dimensional mixed layer ocean model is improved and developed with the capability of representing the dominant processes involved in the development of the diurnal cycle ofsystem.

ACKNOWLEDGEMENTS

This doctoral thesis was accomplished under a NERC studentship for which I am most grateful. I would like to thank my supervisors Prof. Keith Haines and Prof. Nancy Nichols for their wisdom and guidance. I also add thanks to my wife Ann for her patience and understanding during this time, particularly during the nal months.

DECLARATION

I con rm that this is my own work and the use of all material from other sources has been properly and fully acknowledged.

Samuel Pimentel

List of Figures

1.1 A Schematic of ocean-atmosphere processes 2

1.2 A typical upper ocean vertical temperature pro le 6

2.1 Sketch of model grid 22

3.1 Drag coe cient versus wind speed 34

4.1 Arabian Sea observables 39

4.2 An SST comparison using the Kondo and Fairall air-sea ux algorithms . . . 42

4.3 COARE model-observation comparisons 47

4.4 Arabian Sea model-observation comparisons 49

4.5 Temperature depth pro le at Arabian Sea 51

4.6 Subduction model-observation comparisons 53

4.7 Modelled SST at Arabian Sea using observed and parameterised SWR 54

4.8 The e ects of cloud cover over COARE 56

5.1 SST using the direct insertion method 73

5.2 Arabian Sea heat uxes with and without SST

6.1 North Atlantic (30°N, 310°E) SSTs for July 2005 90

6.2 Comparing SST result using prescribed and dynamic uxes 96

6.3 Comparing prescribed and dynamic uxes 97

6.4 Atlantic Ocean diurnal warming map 1^{st} January 2006 100

6.5 Atlantic Ocean diurnal warming map 2^{nd} January 2006 101

6.6 Atlantic Ocean diurnal warming map 3^{rd} January 2006 102

6.7 Atlantic Ocean diurnal warming map 4^{th} January 2006 103

6.8 Atlantic Ocean diurnal warming map 5^{th} January 2006 104

6.9 Atlantic Ocean diurnal warming map 6^{th} January 2006 105

6.10 Atlantic Ocean diurnal warming map 7^{th} January 2006 106

7.1 An illustrat8Td (An)Tj 1m(.)Tj 8.5r55

7.12 Daily Peak SWR at -45°N to -25°N and 300°E to 330°E before and after assimilation 135

List of Tables

4.1 Mooring sites 37

4.2 Modelling results at the mooring sites 1 43

4.3 The mean air-sea uxes at the mooring sites 44

4.4 Di erences between Kondo and Fairall air-sea uxes 45

4.5 Modelling results at the mooring sites 52

4.6 Arabian Sea diurnal warming statistics 55

4.7 COARE diurnal warming statistics 57

4.8 Modelling results from 6 hourly forcing 1 58

5.1 Modelling results and persistence at the mooring sites 70

5.2 Modelling results at the mooring sites 2 80

5.3 Modelling results from 6 hourly forcing 2 80

6.1 TMI and AMSRE error statistics 89

6.2 Turbulent mixing options 94

6.3 Prescribed and dynamic ux values 96

6.4 Atlantic model run comparison to observations 108

6.5 OSTIA comparison to observations 109

7.1 Results from assimilating SST observations into the diurnal cycle 125

7.2 Results from assimilating IR and MW SST observations into the diurnal cycle 126

7.3 Results comparing modelled SST to di erent satellite types 136

7.4 Results comparing day/night match-ups 137

7.5 Results comparing OSTIA to individual satellite types 137

7.6 Results comparing wind observations to ECMWF forecast values 139

List of Abbreviations

AATSR	Advanced Along-Track Scanning Radiometer
AVHRR	Advanced Very High Resolution Radiometer
CMO	Coastal Mixing and Optics Experiment
COARE	Coupled Ocean-Atmosphere Response Experiment
DW	Diurnal Warming
ECMWF	European Centre for Medium-Range Weather Forecasts
EnKF	Ensemble Kalman Filter
ENSO	El Nino Southern Oscillation
ESSC	Environmental Systems Science Centre
FOAM	Forecast Ocean Analysis Model
GCM	General Circulation Model
GHRSST-PP	GODAE High Resolution Sea Surface Temperature Pilot Project
GMT	Greenwich Mean Time
GODAE	Global Ocean Data Assimilation Experiment
GOCE	Geostationary Operational Environment Satellite
GOTM	General Ocean Turbulence Model
HADISST	Hadley Centre Sea Ice and Sea Surface Temperature Data Set
IR	Infrared
JAXA	Japan Aerospace Exploration Agency
LWR	Long-wave Radiation
MLD	Mixed Layer Depth
MOST	Monin-Obukhov Similarity Theory
MW	Microwave
NAR	North Atlantic Regional

NASA	National Aeronautics and Space Administration
NCAR	National Center for Atmospheric Research
NCOF	National Centre for Ocean Forecasting
NWP	Numerical Weather Prediction
OI	Optimal Interpolation
OSTIA	Ocean Sea Temperature and Ice Analysis
PDE	Partial Di erential Equation
POLCOMS	Proudman Oceanographic Laboratory Coastal Ocean Modelling System
RMS	Root Mean Square
RSOI	Reduced Space Optimal Interpolation
SeaWiFS	Sea-viewing Wide Field-of-view Sensor
SEVIRI	Spinning Enhanced Visible and Infrared Imager
SST	Sea Surface Temperature
STD	Standard Deviation
SWR	Short-wave Radiation
TKE	Turbulent Kinetic Energy
TMI	TRMM Microwave Imager
TOGA	Tropical Ocean Global Atmosphere
TRMM	Tropical Rain Measuring Mission
UKMO	United Kingdom Meteorological O ce
WHOI	Woods Hole Oceanographic Institute

List of Symbols

	Buoyancy
c_p	Specific heat capacity of sea water at constant pressure
c_{pa}	Specific heat capacity of air at constant pressure
c, c'	Stability functions
	Water vapour pressure
	Gravitational acceleration
	Height above sea surface
$_i$	Thichness of model grid layer i
	Turbulent kinetic energy; thermal conductivity of sea water
	Generic length scale
n	Fractional cloud cover
p	Sea water pressure
	Water vapour mixing ratio
$_{rh}$	Relative humidity
$u = (,)^T$	Horizontal wind velocities
$_*, _*, _*$	Scaling parameters
$v = (,)^T$	Horizontal sea water velocities
	Depth in the water column
$_0, _0, _{0T}$	Roughness lengths
$_{MLD}$	Mixed layer depth
$_i$	Depth at model grid layer i
A_a	Water vapour and ozone absorption
	Production of turbulent kinetic energy by buoyancy
C_D, C_E, C_H	Transfer coefficients for momentum, latent and sensible heat respectively
C_n	Cloud cover coefficient used in Reed formula

0	Net surface short-wave radiation
$\downarrow$	Clear Sky Surface insolation
di	Surface di use insolation
dir	Sur ace direct insolation
L	Mo n-Obukhov length
Lv	L

λ_n	Latitude dependent cloud cover coe cient
	Sea water density
$_0$	Reference sea water density
$_a$	Air density
	Stefan-Boltzmann constant
$_{k,}$	Schmidt number for turbulent kineticer

Chapter 1

Introduction

M n

Knowledge of sea surface temperatures (SSTs) has importance for humankind with many valuable social and economic bene ts. The SST is a crucial component in many physical, biological, and chemical processes within the Earth system. It is one of the most important properties governing the exchange of energy between the atmosphere and ocean and as such is of paramount importance in air-sea ux calculations. A good knowledge of SST is therefore germane in our understanding of upper ocean physical, biogeochemical processes, and air-sea interaction. SST is a variable widely used for describing ocean circulation and dynamics. It has an important role in Numerical Weather Prediction (NWP) as a boundary condition in General Circulation Models (GCMs) and therefore is valuable for weather forecasting. For example a necessary condition for the genesis of tropical cyclones is that the SST be above approximately 26 $^\circ$C and SST maps are used to evaluate oceanic heat content, which is important for predicting hurricane intensity development [126] and [45]. It also has an important role in climate science where it is viewed as a key indicator of climate change and variability [53].

A n c n

The SST may be perceived as being determined by a balance of many processes, including air-sea exchange, ocean transport, and ocean mixing. Figure 1.1 illustrates these principal environmental processes that affect SST. An understanding of these processes and their interactions is vital for the beneficial inclusion of global high resolution SST observations into ocean models.

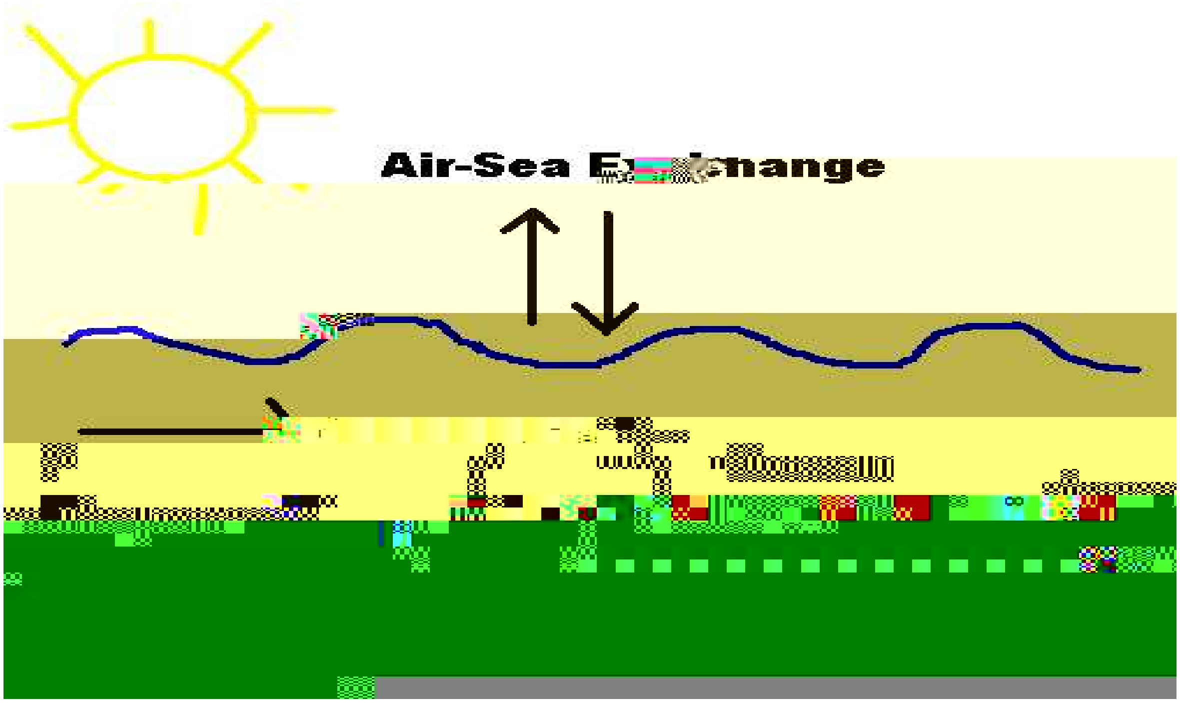

Figure 1.1: A schematic diagram illustrating the various processes that influence SST in the ocean-atmosphere system.

3 c n c

The heat budget of the oceanic mixed layer represents a balance of several terms [132]

$$z_{MLD}\frac{\partial \ _a}{\partial t} + z_{MLD}(v_a.\nabla \ _a + \overline{v'_a \cdot \nabla \ '_a}) + (\ _a - \ _{z_{MLD}})w_e + \nabla \cdot \int_{z_{MLD}}^{0} \hat{v}_a \hat{\ }_a dz = \frac{Q + Q_{z_{MLD}}}{c_p}. \quad (1.1)$$

From left to right the terms represent, local storage, horizontal advection (split into mean and eddy terms), entrainment, vertical temperature and velocity covariance, and the combination of net atmospheric heating and vertical turbulent diffusion at the base of the mixed layer, where z_{MLD} is the mixed layer depth, θ_a and $v_a = (u_a; v_a)^T$ are the mixed layer depth averaged sea temperature and horizontal velocities, over-bar represents a time mean, θ'_a and v'_a are deviations from the mean, $\hat{\theta}_a$ and $\hat{v}_a$ represent deviations from the vertical average. The entrainment velocity w_e can be replaced by $\frac{\partial z_{MLD}}{\partial t} + \nabla \cdot z_{MLD} v_a$ following [132]. The net surface heat flux without solar radiation, denoted Q, can be split into the following

$$Q = Q_E + Q_B + Q_H. \tag{1.2}$$

From left to right these components represent the latent heat flux, the net surface long-wave radiation and the sensible heat flux, with units Wm^{-2}. The term $Q_{z_{MLD}}$ can be separated as follows

$$Q_{z_{MLD}} = I_0 - I_{z_{MLD}} + \rho c_p \overline{w' \theta'_{z_{MLD}}}, \tag{1.3}$$

where I_0 denotes the net surface solar radiation, with units Wm^{-2}. The mixed layer does not absorb all of I_0, a fraction $I_{z_{MLD}}$ penetrates below depth z_{MLD}. The final entry is turbulent diffusion at the base of the mixed layer.

Simplifications to this complete heat budget and a more in-depth look at the various sources and sinks are presented in Chapter 3.

4 s f ns

se s

A limited number of in-situ observations of SST are available from ocean moorings, buoys, and ship observations. Argo floats [47] provide vital profile information of temperature and salinity needed to initialise ocean models. In this thesis a few research moorings providing intensive periods of observations are used to validate an ocean model and develop assimilation routines.

e e e ed

SST measured from Earth observation satellites is increasingly required for use in the context of operational monitoring and forecasting of the ocean, for assimilation into coupled ocean-atmosphere model systems and for applications in short-term NWP and longer term climate change detection. The wealth of satellite SST data now available for scienti c research opens the possibility of large improvements to SST estimation. Currently there are many di erent operational SST data products available; most are derived at least in part from satellite systems [106]. Space borne SST observations are derived from brightness temperatures as measured by infrared (IR) or microwave (MW) radiometers. The performance of infrared radiometers is hampered by cloud cover, whereas the microwave radiation is able to propagate through clouds, but observations can be contaminated by heavy rainfall (see Section 6.3 for more information).

n y

The optimal use of such data, however, is not straight forward. Donlon et al [32] discusses the di culties in validation of satellite SST measurements; they argue that a better understanding of the spatial and temporal variability of thermal strati cation of the upper-ocean layers especially during low-wind speed peak, after which the amplitude decays as surface co spatial structure. The SST at 5 metres (the depth at the centre of the top grid box

The diurnal cycle is a fundamental signal in the climate system [157]. Increasingly which then have a feedback effect on future SSTs. NWP and climate simulations use standard SST datasets such as Reynolds et al [111] which produce monthly or weekly mean fixed bulk SSTs. These SSTs are used in the calculation of the air-sea fluxes. This process can lead to two sources of errors. Firstly the bulk SST is not the temperature at the interface and therefore should not be used in any flux calculations; earlier we noted that skin to bulk temperature differences can be significant. This is something that was addressed by Fairall et al [35] who developed a bulk flux algorithm that incorporated a warm layer and cool skin effect (see Section 3.5.8). The second source of error stems from the use of mean SST values which smooth out any diurnal variations in SST. Ledvina et al [75] showed that monthly, weekly, and daily averaged bulk meteorological parameters can lead to serious errors in fluxes especially in equatorial, temporally variable wind regimes. In another study in the western Sargasso Sea by Cornillon et al [23], they found that diurnal effects produced a monthly mean SST that was $0.2\,^{\circ}\mathrm{C}$ higher and resulted in a decrease of $5\,\mathrm{W m^{-2}}$ in the mean heat flux entering the ocean. Webster et al [151] reveal that a $1\,^{\circ}\mathrm{C}$ change (or error) in SST would result in a change (or error) of $27\,\mathrm{W m^{-2}}$ in the net o e e s s ed L ye e

sides of a horizontal SST discontinuity experience identical clear sky, low wind speed conditions, then the warmer side will produce a weaker diurnal SST signal than the cooler side. This is because on the warmer side the greater SST will cause a larger heat release (resulting from long-wave radiation and latent and sensible heat ux losses) from the ocean and thus dampen diurnal warming when compared with the colder side of the front. Thus, in this situation, remotely sensed data of the sea surface taken during the day would reveal a much reduced or even vanished horizontal gradient when compared to the initial (pre diurnal warming) horizontal gradient. However, the true horizontal gradient would still be present below the shallow diurnal thermocline. This masking or camou aging of horizontal gradients in remotely sensed SST data could have adverse e ects for users of such data e.g. the shing industry, in the estimation of acoustic transmission, and the forecasting of hurricane development.

n y M ng

Attempts to model the upper ocean response to diurnal heating, cooling, and wind mixing are limited in number. Accurately modelling diurnal variability is di cult as it involves the complex non-linear interaction between ocean and atmosphere. However, attention should focus on a few core issues: the choice of mixing parameterisations, ux forcing resolution, vertical grid resolution, and the penetration of solar radiation. In this section a review of studies that have speci cally focused on modelling the diurnal cycle of SSTs is presented, focusing on the above issues.

The rst detailed modelling study of the diurnal cycle was by Price et al [104] who developed a bulk model dependent on the generation of shear instability at the base of the mixed layer. This model was also used by Shinoda to model diurnal variability in the western equatorial Paci c [128] and [127]. Hallsworth [50] compared the Price bulk mixed layer model with a turbulence closure model called GOTM (See Chapter 2) at two mooring sites and consistently found GOTM performing better at modelling the diurnal cycle of near surface temperatures. An alternative earlier bulk model by Kraus and Turner [72] was compared to the di usion model of Kantha and Clayson

[62] in a study on modelling odiurnal TjH369.5837n

exponentially to 60 cm at the 60th layer, when comparing model output to AATSR observations. Hallsworth [50] had a vertical grid with thickness of order centimetres near the surface decreasing to order metres at deeper depths.

Another area of importance for diurnal cycle modelling is the penetration of solar radiation into the ocean (see Section 3.3). In [104] they used a parameterisation by Paulson and Simpson [100] (see Section 3.3). This parameterisation is still widely used in diurnal modelling studies e.g. [9] and [127] in spite of its inappropriateness for accurate representation of diurnal warming, presumably because it is still used in the majority of current climate models. Improvements are, however, made by Horrocks et al [52] who implement the more appropriate 9 band parameterisation [101]. Hallsworth [50] experimented with several parameterisations including decomposing the full spectral range into 278 interv

represent temperatures at the skin and

from the work. Areas for further research that could build on the foundations laid in this thesis are also identi ed.

Chapter 2

The Model

n c n

One-dimensional modelling of the oceanic mixed layer has been widely used in the development of turbulence and air-sea ux parameterisations. Full scale ocean and climate models are computationally expensive and are time consuming to run; thus an advantage of the single column model is the ability to perform multiple model simulations in a relatively short amount of time. The oceanic mixed layer model also has reduced complexity and size which allows the user to become fully acquainted with the model. These characteristics provide the malleable framework for testing parameterisations. One-dimensional mixed layer models are particularly suitable for modelling the diurnal variability of SST because much greater near surface vertical resolution can be achieved compared with larger ocean models where computational limits are apparent. This ne vertical resolution is essential for the ability to capture the diurnal thermocline which is of paramount importance in estimating SST over diurnal time-scales, whereas the horizontal scales of three-dimensional ocean models are of limited importance in the development of the diurnal cycle of SST.

Vertical exchange processes across the air-sea boundary, as well as vertical mixing within the water column, are likely to a ect the local conditions much more rapidly and e ectively than horizontal advection and horizontal mixing [93]. This is the assumption adopted when using a one-dimensional model where horizontal gradients are

and Neumann type (ux) surface and benthic boundary conditions

$$({}_t + {}^m)\frac{@v}{@z} = \frac{1}{{}_0}\tau \quad \text{at} \quad z = 0 \qquad \text{and} \qquad ({}_t +)\frac{@v}{@z} = 0 \quad \text{at} \quad z = -H; \quad (2.7)$$

$$({}'_t +)\frac{@}{@z} = \frac{1}{c_p \ {}_0}Q \quad \text{at} \quad z = 0 \qquad \text{and} \qquad ({}'_t +)\frac{@}{@z} = 0 \quad \text{at} \quad z = -H; \quad (2.8)$$

$$({}'_t + {}^S)\frac{@S}{@z} = 0 \quad \text{at} \quad z = 0 \qquad \text{and} \qquad ({}'_t + {}^S)\frac{@S}{@z} = 0 \quad \text{at} \quad z = -H: \quad (2.9)$$

The rst terms on the right hand sides of equations (2.1), (2.2), and (2.3) generate the mixing. Fixed values have been prescribed for the molecular di usivities of momentum, heat, and salt denoted ^{m}, , and ^{S} respectively. The computation of the turbulence di usivity parameters ${}_t$ and ${}'_t$ is discussed in Section 2.3.

Bottom friction is treated implicitly using the second term on the right hand side of equation (2.1).

The source term in equation (2.2) and the surface boundary conditions (2.7) and (2.8) are discussed in detail in Chapter 3. The reference sea water density (1025 kgm structures arise called eddies. Eddy motion is complex and the details little understood, however stochastic average properties of the ow (averages over many realisations in statistical theory) can be formulated [145].

e e gy

To complete closure of equations (2.1), (2.2), and (2.3) we need to compute the turbulence parameters $_t$ and $'_t$. As described in [145hastic aed e e g

The k{ 2-equation turbulence model has been modi ed such that the analytical concept of a wave-enhanced layer located on top of the classical law-of-the-wall layer is reproduced. This follows work by Craig and Banner [24] who suggested modelling the ux of TKE due to breaking waves into the water column as proportional to the cube of the surface friction velocity. In order to implement this parameterisation into the k{ 2-equation turbulence model, Burchard [11] modi ed two features of the dissipation rate equation for : the surface boundary condition and the turbulent Schmidt number . It should be noted that wave breaking should only be used in conjunction with near surface resolution of O(cm), and that the physics of this region of complex dynamics is still in its infancy63.485 0 Td (this)Tj16.3

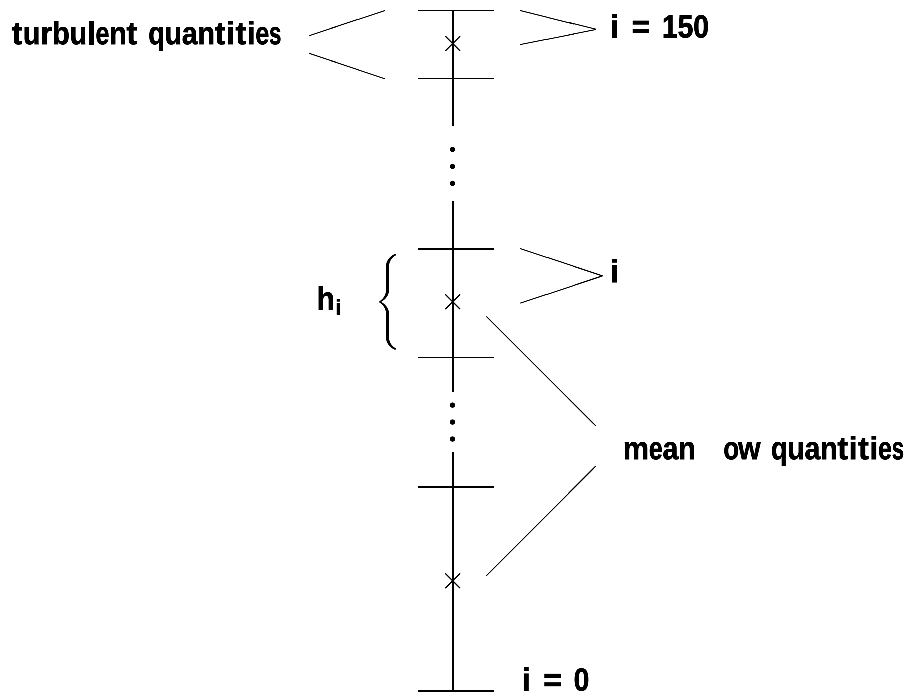

Figure 2.1: A sketch of the model grid made up of 150 non-uniform layers.

Equations (((P)Tj 1 0 0 1 377.52 60Rp 0 0 -ces150

$$\frac{X_i^{n+1} - X_i^n}{\Delta t} = \frac{\nu_i^n \left(\frac{X_{i+1}^{n+\theta} - X_i^{n+\theta}}{\frac{1}{2}(h_{i+1} + h_i)} \right) - \nu_{i-1}^n \left(\frac{X_i^{n+\theta} - X_{i-1}^{n+\theta}}{\frac{1}{2}(h_i + h_{i-1})} \right)}{h_i}; \tag{2.22}$$

$$\frac{X_1^{n+1} - X_1^n}{\Delta t} = \frac{\nu_1^n \left(\frac{X_2^{n+\theta} - X_1^{n+\theta}}{\frac{1}{2}(h_2 + h_1)} \right) - F_b}{h_1}; \tag{2.23}$$

for $1 < i < 150$, where the layer thickness h_i is given in Equation (2.17). The semi-implicit time level is defined by

$$X^{n+\theta} = \theta X^{n+1} + (1 - \theta) X^n. \tag{2.24}$$

The value of θ is chosen to be 0.6 which is slightly more implicit than the Crank and Nicolson scheme [25], in order to obtain asymptotic stability. Because of the implicit treatment of vertical diffusion and the absence of advection there are no limitations by Courant numbers. The resulting linear system of equations (2.21) – (2.23) has a tri-diagonal matrix structure which is solved by means of the Thomas algorithm (a simplified Gaussian elimination).

The numerical discretisation of equations (2.12) and (2.15) are slightly different from those above, due to the constraint that turbulent quantities are generally non-negative. Equations (2.12) and (2.15) can be written in the simple form,

$$\frac{\partial X}{\partial t} = P - QX; \quad P, Q > 0; \tag{2.25}$$

with X denoting a non-negative quantity, P a non-negative source term, QX a non-negative linear sink term, and t denoting time. P and Q depend on X and t. A simple discretisation of (2.25) would be

$$\frac{X^{n+1} - X^n}{\Delta t} = P^n - Q^n X^n; \tag{2.26}$$

which to keep the solution positive would require an unreasonable time step restriction of

$$\Delta t < \frac{X^n}{X^n Q^n - P^n}. \tag{2.27}$$

Therefore a quasi-implicit numerical procedure [99] is applied

$$\frac{X^{n+1} - X^n}{\Delta t} = P^n - Q^n X^{n+1}; \tag{2.28}$$

which always yields a non-negative solution for X^n

Chapter 3

The Forcing

3 n c n

The dynamic coupling of oceanic

as follows. The surface insolation under clear skies may be split into a direct and di use component

$$I_{\downarrow} = I_{dir} + I_{di} \; : \tag{3.1}$$

These components are then calculated following the approach of Rosati and Miyakoda [116]. The direct component is written as

$$I_{dir} = S_0 \cos(!) \quad ^{\sec(!)}; \tag{3.2}$$

where S_0 denotes the solar constant estimated to be around 1370 Wm^{-2}, and ! is the solar zenith angle (the angle measured at the earth's surface between the sun and the zenith). The cosine of the solar zenith angle can be written as

$$\cos(!) = \sin(\;)\sin(\;) + \cos(\;)\cos(\;)\cos(h); \tag{3.3}$$

where denotes latitude, denotes the sun declination angle (the angle between the Earth-sun line and the equatorial plane), and h denotes the sun's hour angle (which is the angular distance, expressed in hours, minutes, and seconds (one hour equals 15 degrees), measured westward along the celestial equator from the observer's celestial meridian to the hour circle of the object being located). Finally (in Equation (3.2)) denotes the atmospheric transmission coe cient which represents the attenuation of I_{dir} by the atmosphere and is set at 0:7. The di use clear sky radiation has been approximated by

$$I_{di} \; = ((1 - A_a)S_0 \cos(!) - I_{dir}) = 2: \tag{3.4}$$

This says that when scattering occurs, half is scattered downward and the other half back. A_a represents water vapour and ozone absorption taken to be 0:09. Next a modi cation to $I_{\downarrow}$ due to cloud cover is needed. A comparative study of these methods by Dobson and Smith [31] found that the Reed formula [109] gave the best long-term mean insolation values. The Reed formula has been widely used in the oceanographic community and is surprisingly accurate for such a simple expression [97]. The Reed formula is as follows

$$I_0 = I_{\downarrow}(1 - C_n n + 0:0019 \;)(1 - \;); \tag{3.5}$$

where n is the fractional cloud cover, c_n the cloud cover coe cient set as 0.62, the solar noon angle, and the albedo calculated as a function of sun altitude as described by Payne [102]. This formula is used only for 0:3b

the incident surface irradiance that exists at depth. This can be parameterised as a sum of exp

ozone), aerosols, and clouds. The up-welling radiation is emission from the sea surface, depending on surface emissivity and $_{skin}$, augmented by a small contribution due to re ection of the down-welling LWR. Therefore we have

$$Q_B = \quad {}^{4}_{skin} - (1 - \quad {}_{L})\, Q_B^{\downarrow}: \tag{3.9}$$

The largest component is the up-welling part, which is most accurately computed using the Stefan-Boltzmann Law, ($\;^{4}_{skin}$) where is the surface emissivity taken to be 0:98, is the Stefan-Boltzmann constant ($5{:}67 \times 10^{-8}\,\mathrm{Wm^{-2}K^{-4}}$), and $_L$ is the long-wave re ectivity taken to be 0:045. To compute the LWR either measured observations of $Q_B^{\downarrow}$ (the down-welling component) from a pyrgeometer can be used, or Q_B can be obtained from operational analyses. Alternatively the LWR can be parameterised; in GOTM a formula by Clark is [21]:

$$Q_B = \quad {}^{4}_{skin}(0{:}39 - \ldots\, n^2) \ldots {}^{3}_{skin}({}_{ski} \ldots T_a); \tag{3.10}$$

where e is the water vapo ... e ai ... fractional cloud cover, T_a ... K ... d ... a la ... de ... en ... cloud cover coe cient. ... isa ... ten ... t, ... review by Katsaros [65] ... Equatio ...) to ... ost ... urat ... it ... only $-5{:}5\,\mathrm{Wm^{-2}}$. More re ... ame ... s by ... mi ... an ... ose ... have been shown to be4 ey d s A e ges

This is a technique that allows us

Using the above theory, we are now able to express our turbulent uxes for wind stress $\tau = (_x; \ _y)$

$$\frac{h}{T_*}\frac{\partial < T_a >}{\partial h} = \ _T: \tag{3.20}$$

The quantities in angular brackets represent mean values in time, denotes the von Karman constant, and $_i$ are functions of the stability parameter $= h=L$, where L is the Monin-Obukhov length de ned as

$$L = \frac{T_v|u_*|^3}{g \ \langle w' T_v' \rangle}; \tag{3.21}$$

co ireac

T_v denotes the virtual air temperature and h the height above the surface. Integrating (3.18) { (3.20) from the surface to the measurement height gives

brac w 11.9552 Tf 4.56001 1.8 Td ())Tj 7.7

$$u(h_u) = u_s + \frac{u_*}{}\left[\ln\left(\frac{h_u}{z_0}\right) - \ _m\right]; \tag{3.22}$$

76j /R76 7.97011 Tf 9.13064 -1.8 Td (m)T

$$q(h_q) = q_s + \frac{q_*}{}\left[\ln\left(\frac{h_q}{z_{0q}}\right) - \ _q\right]; \tag{3.23}$$

$$T_a(h_T) = \ _{skin} + \frac{T_*}{}\left[\ln\left(\frac{h_T}{z_{0T}}\right) - \ _T\right]; \tag{3.24}$$

where the functions $_i$ (the integrals of $_i$) are stability corrections to the pro le. The quantities z_0, z_{0q}, and z_{0T} are the roughness lengths (the heights at which the extrapolation of the logarithmic pro les reach the respective surface value under neutral conditions, see [98] or [73] for discussions on this topic).

Therefore using equations (3.22) { (3.24) together with equations (3.15) { (3.17) the transfer coe cients can be written as

$$C_D = \ ^2\left[\ln\left(\frac{h_u}{z_0}\right) - \ _m\right]^{-2}; \tag{3.25}$$

h_u

$$C_E = \ ^2\left[\ln\left(\frac{h_q}{z_{0q}}\right) - \ _q\right]^{-1}\left[\ln\left(\frac{h_u}{z_0}\right) - \ _m\right]^{-1}$$

Therefore { (3.17)

thewher38 11.9552 Tf 12.4698 0 Td ( )Tj /R70 H3 11.9552 Tf 7.91997 18 Td (2)Tj /R153 11.955

d

Deriving parameterisations to calculate air-sea uxes is very di cult. Many approximations are needed and much of the physics is not well understood. A plethora of di erent approaches have been developed and implemented over the years. A good reference guide to many of the methods is presented in [97]. In the public domain version of GOTM the method of Kondo [71] is used. In this method the transfer coe cients under neutral conditions are approximated by a quadratic function of the 10 metre wind speeds. These are then used together with an approximate stability formula to nd the transfer coe cients proper. Much advancement in the science of parameterising turbulent uxes has been achieved since Kondo's publication. Therefore we implemented a more recent and advanced algorithm (see Section 3.5.8 below) into GOTM.

A COA A g

A newer scheme devised and updated by Fairall et al, ([37] and [36]) for the TOGA COARE region has been found to be accurate within 5% for wind speeds of 0{10 ms^{-1} [36], and is considered state-of-the-art. This scheme was studied and implemented into GOTM as an alternative to Kondo.

The algorithm is based on the Liu-Katsaros-Businger [76] method with the added sophistication of a skin SST [35], (the true interface temperature), and a gustiness velocity factor to account for sub-grid scale variability.

The transfer coe cients are computed using an iterative cycle where scaling parameters and stability In

11f75 9485

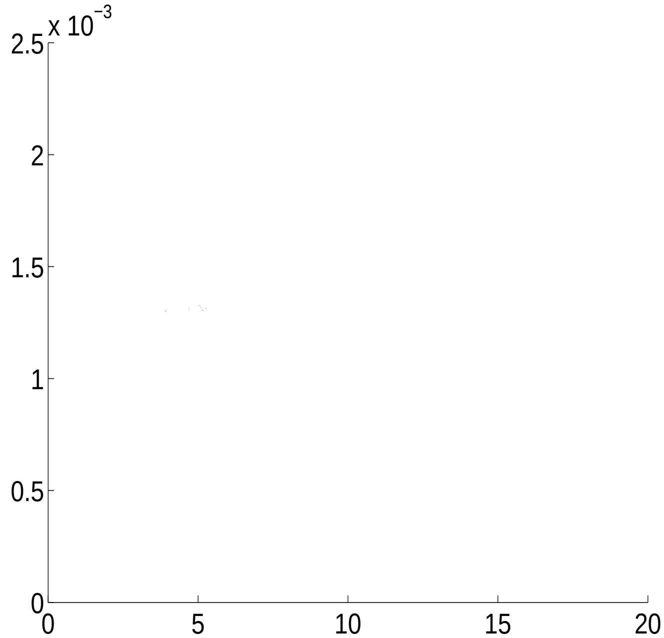

x 10^−3
2.5
2
1.5
1
0.5
0
0
5
10
15
20

where is an empirical coe cient, is the kinematic viscosity of water, and u_* is the friction velocity of the water. The di culty comes in estimating . Saunders initially estimated a value between 5 and 10. More recently Fairall et al [35] developed a with a dependence on wind speed including a smooth transition from a shear-driven to a free convection regime as wind speeds asymptote to zero. The skin temperature represents the true interfacial temperature at which heat exchange between the ocean and atmosphere occurs, and thus its inclusion in air-sea ux algorithms was an important development [35]. This cool skin parameterisation is used in the TOGA COARE air-sea ux algorithm described above.

4 M ng s

Meteorological and sea temperature observations are obtained from the Woods Hole Oceanographic Institute (WHOI) upper ocean mooring data archive; this is publicly available at [5]. Work presented here uses time series from three of these deployments. Details of the locations, duration, and frequency of data for each time series is given in Table 4.1. The meteorological variables consist of the wind speed components u and v, air temperature T_a, relative humidity q_{rh}, and air pressure of platforms and sensors. A surface mooring was deployed during the COARE intensive observation period for the determination of surface uxes and upper ocean structure near the centre of the warm pool [154]. This warm pool region has been under intense scrutiny because of its importance in world climate [152]; over a decade of work has greatly increased our understanding of this region [44]. One dimensional mixed layer models using this data have contributed to several of these studies e.g. [151], [2], and [128].

Arabian Sea Site

A moored array was deployed in the Arabian Sea in order to improve understanding of air-sea interaction in the region, and in particular to investigate the oceanic response to the strong, large-scale atmospheric forcing associated with the summer and winter monsoons. A full accSea5.c200.9823 0 (to)T j(it)2nsio26.9746 0 Td (ha)ctureric

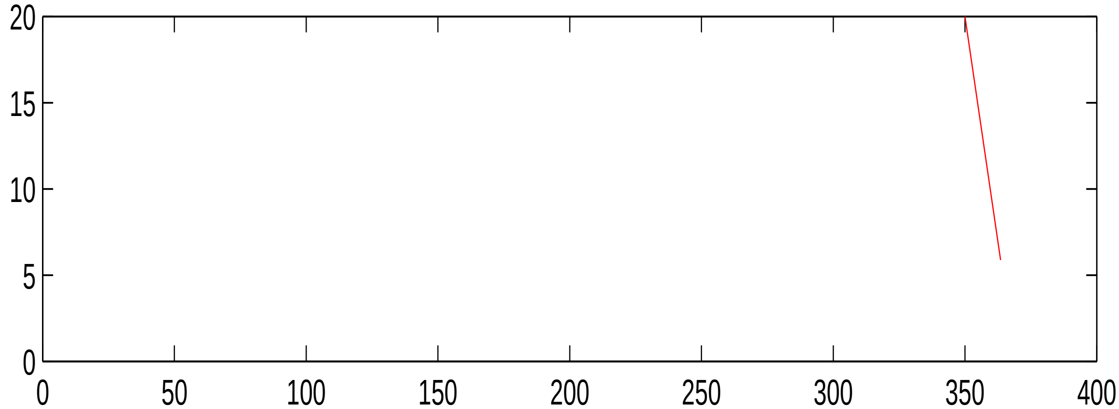

0
5
10
15
20
0
50
100
150
200
250
300
350
400

4.3 M ng c n

This chapter presents modelling results at the three mooring sites. The ability of the model to replicate the sea temperature records, given the observed forcing, can be assessed in various ways. Comparisons are made between the observed and modelled sea temperatures at various or all depths in the water column. Particular interest is paid to the depth of the shallowest measurement (0:45, 0:17, and 1:0 metres at COARE, Arabian Sea, and Subduction respectively) and the ability to model the near surface variability. In this thesis the magnitude of diurnal warming is de ned as the maximum SST (at the shallowest observed depth, z_1^{obs}) minus the minimum SST over a 24 hour window starting at 00:00 GMT

$$z^{\mathrm{obs}} = \max_{0-24} z^{\mathrm{obs}} - \min_{0-24} z^{\mathrm{obs}}: \qquad (4.1)$$

A diurnal warming signal of zero is given if the SST at the start remains the maximum over the day; this eliminates to the maximum modelled depth, $z = 150$ m, and then integrating again over different times, T, to give the evolution

$$c_p \ {}_0 \int_0^T \int_{150}^0 \frac{\partial}{\partial t} dz dt = \int_0^T I + Q dt. \qquad (4.3)$$

The two sides of this equation were evaluated from model results at the three mooring sites over the whole time series giving values of 3.2×10^8 Jm^{-2} at COARE, 2.1×10^9 Jm^{-2} at Arabian Sea, and 4.8×10^8 Jm^{-2} at the Subduction site. The balance of both sides of Equation (4.3) demonstrates that the model conserves heat entering and leaving through the surface boundary. Another comparison is made by comparing the left hand side of Equation (4.3) evaluated using observed temperatures and modelled temperatures (see Section 4.5). This is not expected to be identical as the complete H27.8096 as

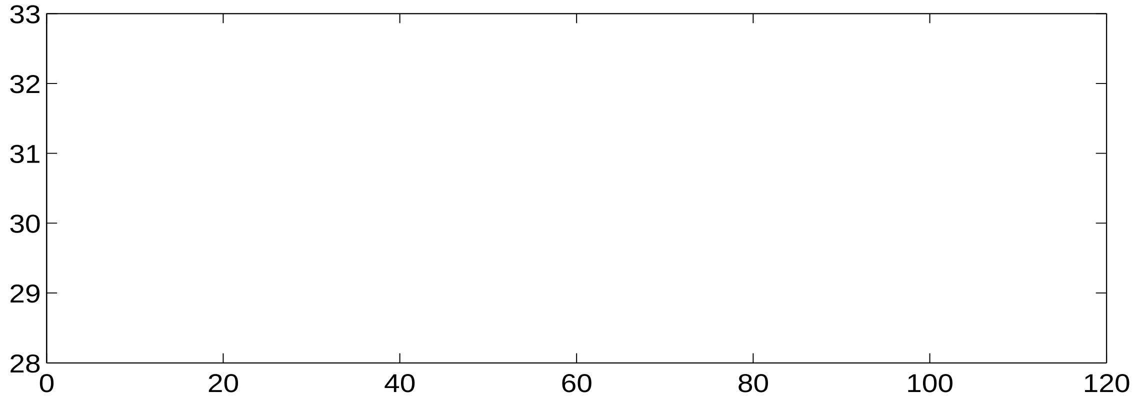
33
32
31
30
29
28
0
20
40
60
80
100
120

		RMS Errors		
Site	Flux Scheme	SST	Diurnal Warming	Strati cation
COARE	Kondo	0.36	0.36	0.25
COARE	Fairall	0.29	0.36	0.22
Arabian Sea	Kondo	1.15	0.28	0.26
Arabian Sea	Fairall	0.71	0.26	0.23
Subduction	Kondo	0.48	0.17	0.14
Subduction	Fairall	0.66	0.18	0.14

Table 4.2: Statistics from comparisons derived from observation4rb5565.28 cm BI /IM80ons

these are presented in Tables 4.3 and 4.4. The values in these tables are calculated from hourly output. The mean air-sea flux values over the whole observational time-series at each mooring site, as shown in Table 4.3, are different for the two algorithms. The Fairall values are generally smaller in each case. The largest difference occurs in the sensible heat flux, which on average over the three mooring sites is 39% smaller for the Fairall estimate compared to Kondo. The root mean square differences between the two schemes as shown in Table 4.4 are also relatively large. Again this is particularly true for the sensible heat flux where the differences between the Fairall and Kondo scheme can be over 50% of the mean value.

		Mean Values		
Site	Flux Scheme	Q_E (Wm^{-2})	Q_H (Wm^{-2})	$\|\tau\|$ (Nm^{-2})
COARE	Kondo	$-101{:}99$ ($-102{:}42$)	$-10{:}44$ ($-10{:}49$)	0.05 (0.05)
COARE	Fairall	$-104{:}38$ ($-102{:}94$)	$-7{:}87$ ($-7{:}57$)	0.04 (0.04)
Arabian Sea	Kondo	$-124{:}31$ ($-142{:}21$)	7.32 ($-3{:}09$)	0.1 (0.1)
Arabian Sea	Fairall	$-107{:}32$ ($-111{:}06$)	0.48 ($-0{:}44$)	0.1 (0.1)
Subduction	Kondo	$-119{:}65$ ($-116{:}39$)	$-12{:}6$ ($-9{:}44$)	0.08 (0.08)
Subduction	Fairall	$-117{:}3$ ($-102{:}38$)	$-11{:}57$ ($-6{:}09$)	0.07 (0.07)

Table 4.3: Mean air-sea fluxes (latent heat, Q_E; sensible heat, Q_H; and wind stress, $|\tau|$) calculated using the Kondo and Fairall algorithms. Values in brackets use the observed SST as opposed to the modelled SST to calculate the air-sea fluxes.

The results shown in this thesis use the TOGA COARE algorithm developed by Fairall et al which is widely appreciated as being significantly more accurate [97]. The evidence presented here is limited as no flux observations are available for comparison. However, results from comparing modelled SSTs, from the two flux methods, to observations seem to favour the Fairall algorithm. Results presented in this section also show that the instantaneous differences between the calculated fluxes of the two methods are significant.

errors from 0:76 °C to 0:62 °C. The results at the mooring sites presented in this thesis use the 9-band parameterisation.

M n n

In this section a more detailed analysis of the model results at the three mooring sites is presented. In these experiments the model is initialised with observed sea temperatures at the start of the time series and forced with air-sea uxes calculated from the surface meteorology (Table 4.1) using the Fairall air-sea ux algorithm, together with downwelling SWR and LWR observations every 15 minutes.

COA

Given in Figure 4.3 are plots of SST, daily maximum

gains/loses heat and thus causes temperatures to rise/fall faster within the mixed layer.

The evolution of the total column integrated heat content is seen in Figure 4.3 (c). In these heat content plots what is imp

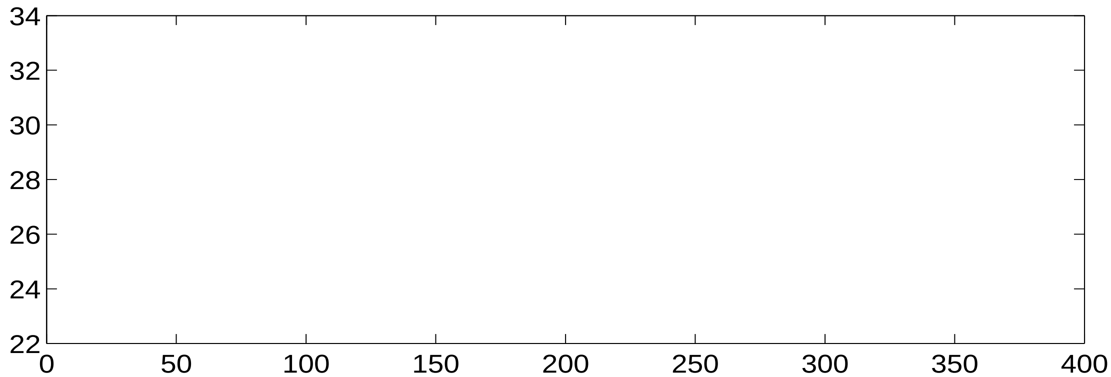
34
32
30
28
26
24
22
0
50
100
150
200
250
300
350
400

to the observed heat content. It is clear that on these occasions the evolution of the modelled and observed heat content are rather di erent. In Equation (4.3) it is shown that the modelled value is determined by the total heat ux $I + Q$, this being the only supply of heat to the system. Here $I + Q$ is calculated from observed down-welling SWR and LWR values with parameterised values of latent and sensible heat ux and up-welling LWR (see Sections 3.4 and 3.5). The use of parameterisations could be a source of potential error in the modelled heat content. However, on the occasions when the two lines in Figure 4.4 (c) signi cantly diverge (e.g. between days 0{10, 25{80, and 270{280) the errors are so large that uncertainties in Q_E, Q_H, and $Q_B^{\uparrow}$ can be ruled out as the major contributing factor to this divergence of heat content. For example, in the rst 10 days the heat content derived from temperature observations increases by approximately $1{:}5 \times 10^9$ Jm^{-2} over the modelled heat content, this would represent an increase in surface heat uxes of over 1700 Wm^{-2} for this period, clearly impossible. However, if advection is important, i.e. $v \cdot \nabla$ is large on these occasions, then our modelling assumption breaks down and we might expect these kinds of di erences.

A paper by Fischer [39] using the same data, in addition to remotely sensed data of the region demonstrates that the observed temperature trend over the whole period is roughly balanced when the heat budget includes the surface forcing, but also strong episodic modulation from mesoscale variability in the horizontal advection. The paper concludes that this mesoscale modulation took two forms, one for each monsoon period. During the NE Monsoon (days 14{121) the heat budget was in uenced by the passage of a series of mesoscale eddies with large variations in thermocline depth, but little surface signature. Then during the SW Monsoon (days 226{333) cool, coastal up-welled water transported to the moored site by mesoscale eddies was deemed a major

Figure 4.6 (a) shows that the modelled SST warms in relation to the observations at around day 150 coincident with a decrease in observed heat content (see Figure 4.6 (c)). Over the whole time series the modelled 1 metre SST has a warm bias of 0:58 °C. The RMS of ($_{1m} - {}^{obs}_{1m}$) over the time series is 0:66 °C, see Table 4.5. The mean diurnal warming signals at this depth are 0:26 °C for the observations and 0:36 °C for the model. The annual deepening and shoaling of the mixed layer is again well represented by the model over this long simulation. In the heat content plot in Figure 4.6 (c) the observed and modelled values of the rst 100 days are closely matched. However after this time the heat content derived from the temperature observations signi cantly decreases with respect to the model derived values, and from this point the model contains much more heat than is observed.

	RMS Errors			
Site	SST (°C)	Diurnal Warming (°C)	MLD (m)	Strati cation (°C)
COARE	0.29	0.36	14.85	0.22
Arabian Sea	0.71	0.26	23.81	0.23
Subduction	0.66	0.18	26.19	0.14

Table 4.5: Statistics from comparisons derived from observations and model simulations at the mooring sites.

In this section an investigation is made into the impact of cloud e ects on the upper ocean. The SWR is the largest component of the ocean heat budget and the amount of radiation received at the sea surface is signi cantly a ected by cloud cover which acts as a barrier preventing the sun's radiation from reaching the sea surface. Cloud cover also in uences the down-welling component of the LWR, as clouds emit thermal infrared radiation.

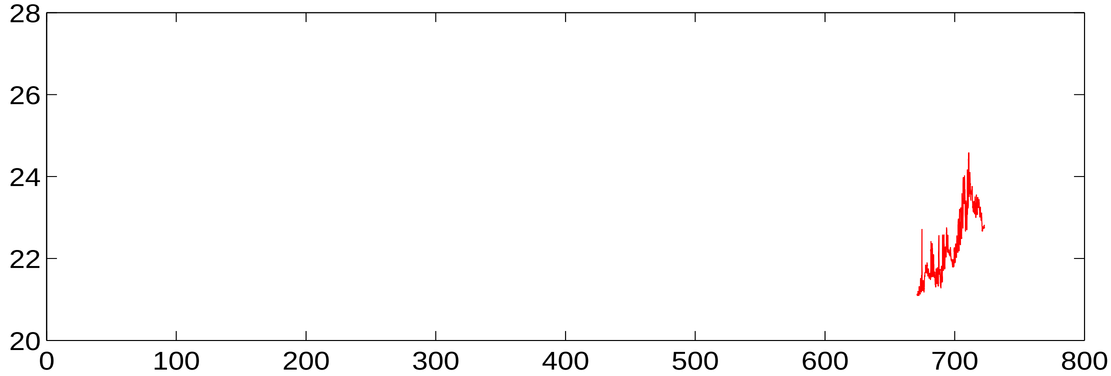
28
26
24
22
20
0
100
200
300
400
500
600
700
800

At the Arabian Sea site the down-welling components of SWR and LWR were observed and this data was used to force the morvthis is primarily caused by advection events at these times.

	Mean Error		RMS Error	
	SST	DW	SST	DW
SWR & LWR Observations	0.13	−0:14	0.71	0.26
SWR Observations	−0:12	−0:15	0.65	0.28
Clear Sky Conditions	−0:66	−0:2	1.17	0.31

Table 4.6: A table showing the modelled SST and diurnal warming (DW) accuracy, in °C, at the Arabian Sea forced with SWR and LWR down-welling observations, SWR down-welling observations with clear sky for LWR, and clear sky conditions for SWR and LWR.

The sensitivity of the model to the cloud parameter can further be seen at the COARE site where SWR values are high, and large diurnal warming events are evident, as shown in Figure 4.8. The day to day variability in the SWR observations (as can be seen in Figure 5.3), primarily due to changes in cloud cover, are large and on occasions over 150 Wm^{-2}, which can be half the daily mean SWR value on some days. If the model is forced with a constant cloud cover [illegible]

SST values are shown in Figure 4.8. It is important not only to notice the drift in SST with zero cloud cover, but also the exaggerated diurnal cycle compared with the observed trends and peaks. The converse is also noted: simulating full cloud conditions leads to an underestimation of SST and its diurnal amplitudes. The mean diurnal warming from observations, clear sky, and full cloud are as follows: 0:48 °C, 0:85 °C, and 0:33 °C. This shows how uncertainty in cloud cover could substantially e ect the modelled diurnal cycle. Error statistics are presented in Table 4.7.

correction (with an e ective mean cloud cover value of 0:30, following [41]) to the clear sky SWR over the whole period. Results from this experiment, shown in Table 4.7, reveal that the SST no longer transmission at the individual sites) and inverting the Reed formula (Equation (3.5))

$$n = \left(1 - \frac{\overline{I_{obs}}}{\overline{I_{\downarrow}}} + 0{:}0019\right) = C_n{:} \tag{4.4}$$

Where over-bar denotes a 6 hourly mean value. This technique allows the SWR to be calculated at a much ner time resolution (at each model time step) with a 6 hourly xed cloud correction performed using the Reed formula. The diurnal cycle of SST is a fundamental response to the solar forcing over the da

Chapter 5

The Assimilation of SST Data

n c n

Data assimilation is the process of merging together in an optimal sense measured observations with a dynamical system model to gain maximum likelihood estimates of the required state. Data assimilation has its theoretical foundations in optimal control theory, a branch of mathematics rst developed by Pontryagin

and these may be expressed as

$$y_k = h_k(x_k) + \ {}_k; \qquad k = 0; : : :$$

The above problem can be solved directly giving a sequential data assimilation scheme, or indirectly to give a four-dimensional variational (4D-Var) assimilation scheme. Using the direct approach the solution can be expressed as (see Kalnay [60] for a derivation)

$$x^b_{k+1} = f_k(x^a_k; u_k); \tag{5.4}$$

$$x^a_{k+1} = x^b_{k+1} + K_k \left(h_k \left(x^b_{k+1}\right) - y_{k+1}\right); \tag{5.5}$$

where

$$K_k = B_k H^T_k \left(H_k B_k H^T_k + R_k\right)^{-1} \tag{5.6}$$

is called the gain matrix and $H_k = \frac{\partial h}{\partial x}\Big|_x$ with $k = 0; \dots; N - 1$. Equation (5.4) represents a prediction for the background states produced from the model equations, and Equation (5.5) represents analysed states based on a correction to the background from mo

This is solved iteratively and each step of the gradient iteration process requires

sub-surface temperature were used to project the surface information into the deep ocean, using data and model error estimates and an optimal interpolation approach to blend model and observed elds.

The UKMO 1° global FOAM has a top grid point temperature representing a mean value over the top 10 metres of ocean. The SST observations used for assimilation come from xed surface buoys (TAU / TRITON), a coarse AVHRR gridded data set, drifting buoys, observing ships, and anything else that comes in over the GTS (Global Telecommunication System, a meteorological agency observations network). An OI assimilation system is used with horizontal and vertical correlation length scales [7].

O e s des

SST

model SST, but retains the observational information in the temporal variability. This is so that observational forcing was not made too strong in the regions where the model SST has a significantly different variance structure. In this 3D-Var assimilation scheme a linear relationship between any two neighbouring depths was derived using singular value decomposition and then applied to estimate the t[illegible]mate lem could not be adequately approached in a one-dimensional framework. They noted that only errors in the air-sea heat ux are accounted for and that other sources of errors such as modelled horizontal advection and diapycnal mixing are not corrected. The results were shown to be particularly poor in shallow areas where the three-dimensional thermal distribution is strongly a ected by tidal excursions and river in ow. Without any horizontal correlations, patches of observational data voids, due to cloud cover led to unrealistic gradients being generated after the assimilation, resulting in the creation of spurious currents on occasions.

es g d y C d s

Traditionally ocean general circulation models are forced by restoring boundary conditions, wherein the top model temperature is restored

(5 metres), $_{2:5m}$ the temperature in the rst layer of the

HadISST

The UKMO Hadley Centre for Climate Prediction and Research (Hadley Centre) Sea Ice and Sea Surface Temperature data set, HadISST1, combines monthly globally complete

likely to be `corrupted' by a diurnal signal. This is clearly not the ideal situation when wind speeds under 6 ms^{-1} account for over 40% of the total occurrence of hourly averaged wind speeds over the ocean (see Figure 2.1 in [79]).

The graphs of Figures 4.3, 4.4, and 4.6 show that the modelled SST on occasions drifts away from the observed SSTs and over or under estimates. The availability of SST observations would allow these errors to be constrained and corrected for. In this next section we use local midnight SST observations in assimilation routines. These data assimilation schemes were developed to use this additional piece of information (the daily SST observation) to improve the state of the system. We seek to achieve this by adjusting the temperature pro le in a physically consistent and smooth manner. The aim is to utilise information content in the observations to highlight shortcomings in model processes and provide insight into how these mat

	RMS Error	
	SST	Diurnal Warming
COARE		
Modelled	0.29	

With $x_k \in \mathbb{R}^{150}$ denoting the sea temperatures at 150 model levels, $u_k \in \mathbb{R}^n$ are the inputs to the system (e.g. surface forcing) at time t_k and $f_k : \mathbb{R}^{150} \times \mathbb{R}^n \rightarrow \mathbb{R}^{150}$ is the discrete nonlinear function describing the evolution of the model temperatures from time t_k to time t_{k+1}. We have a single observation of the SST at time t_k which is related to the state x_k by equation

$$y_k = h_k(x_k); \qquad k = 0; \ldots ; N-1; \tag{5.13}$$

where $h_k : \mathbb{R}^{150} \rightarrow \mathbb{R}$ is a function that maps the state space onto the observation space; in this case a linear grid interpolation from the nearest model grid depths to the observation depth. We then define our state estimator as follows

$$x^a_{k+1} = x^b_{k+1} + K_{k+1}(y_{k+1} - h_{k+1}(x^b_{k+1})); \tag{5.14}$$

for $k = 0; \ldots ; N-1$. The column vector $K_{k+1} \in \mathbb{R}^{150}$ has column entries $K(i)$ defined by

$$K(i) = \begin{cases} 1 & \text{for} \quad z_{MLD} < z^i \leq z^{150} \\ 0 & \text{for} \quad z^1 \leq z^i \leq z_{MLD} \end{cases} \tag{5.15}$$

where z^i represents the model depth at grid level, i, with 150 being the top layer, nearest the surface, and z_{MLD} represents the MLD derived from modelled temperatures as defined in Section 4.3. The SST increment is determined by $y_{k+1} - h_{k+1}(x^b_{k+1})$.

This direct insertion method is based on physical assumptions that the temperatures within the oceanic mixed layer, defined by the depth of the mixed layer at local midnight, are well mixed, so that any temperature signal at the near surface will be merged into the near homogeneous layer through mixing. The SST increment will represent the temperature error throughout the mixed layer. It is assumed that the MLD is correctly known and that the temperature error was caused by incorrect heat fluxes into this mixed layer, whether by advection or surface boundary fluxes. The TKE is

The success of the assimilation method can be viewed in Figure 5.1 where a drift, as shown previously in Figures 4.3,

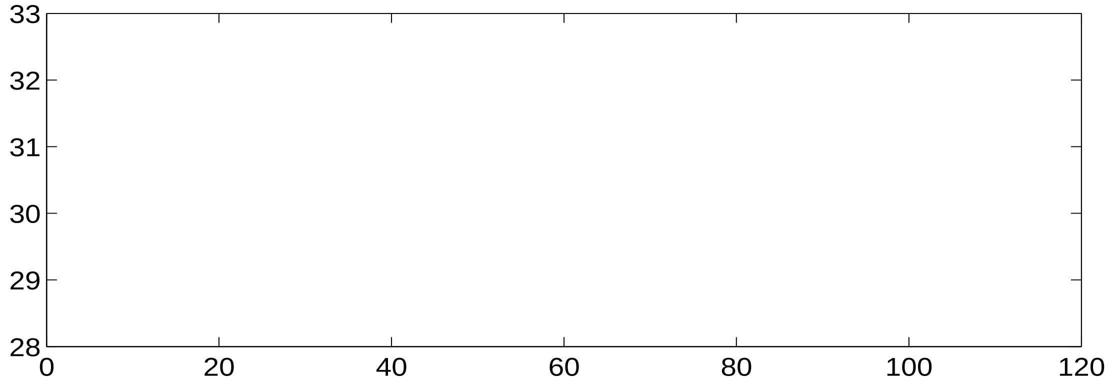
33
32
31
30
29
28
0
20
40
60
80
100
120

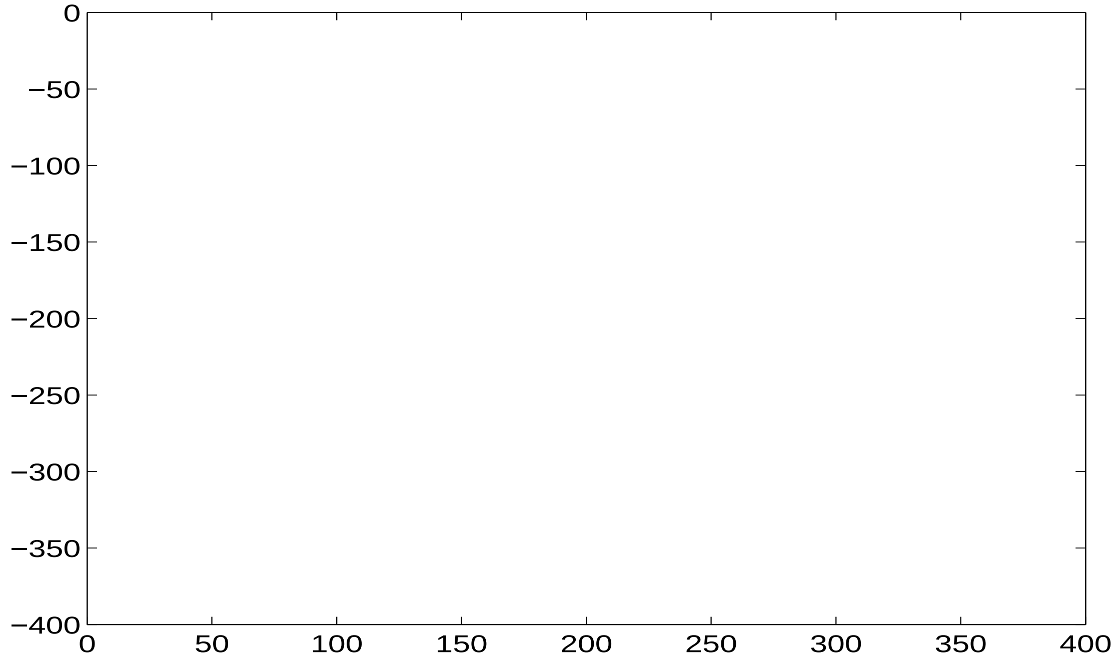
0
−50
−100
−150
−200
−250
−300
−350
−400
0
50
100
150
200
250
300
350
400

is caused by

constraints of the SWR

For the Arabian Sea (Figure 5.4) there are occasions (e.g. days 0{10, 25{40, 40{80, and 270{280) when changes in the 1-D budget are to

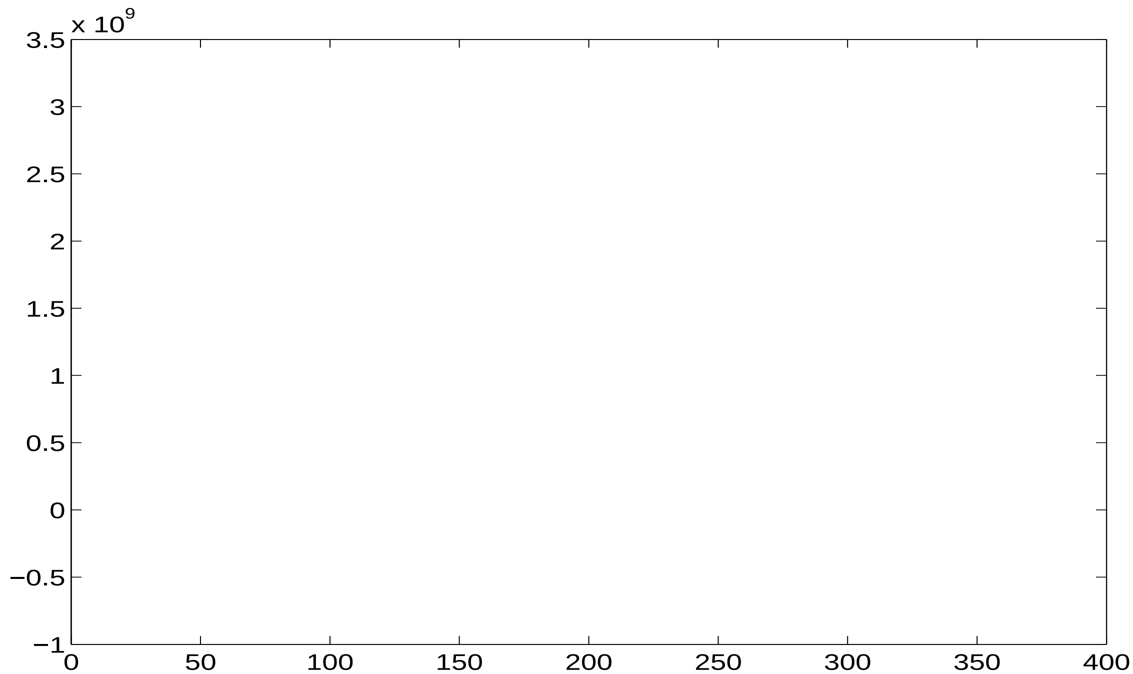
× 10^9
3.5
3
2.5
2
1.5
1
0.5
0
−0.5
−1
0
50
100
150
200
250
300
350
400

	RMS Errors

temperatures, air-sea uxes, and ocean mixing. An example, at the Arabian Sea site, of how the SST assimilation can a ect the MLD is shown in Figure 5.7. As observed in Figure 5.2 at around day 260 there is a large di erence in the sum of LWR and latent and sensible heat uxes calculated by the control run and the model run with data assimilation. This change in the heat ux total produces the shoaling in the MLD at around day 290 and thus better resolves the observed MLD at this time. However, this type of change in the MLD is not seen at other times of the year.

temperatures would b

information is needed in order to constrain ocean heat content. Nevertheless a series of SST observations in time may contain information on the depth of the true mixed layer, although how this could be utilised was not established. A major problem with some of the assimilation methods developed in this chapter was the attribution of error to a single cause. At these various sites and at di erent times numerous sources of temperature errors have been identi ed. These include advection, cloud cover, and incorrect MLDs; however, it is very di cult to attribute a single daily SST error to a particular process. Therefore at this stage the best that can be done is to make corrections to mixed layer temperatures based on SST measurements, and whenever possible use pro le information to improve initialisation. In Chapter 7 it is shown how SST observations taken over the day can be used to improve the modelled estimation of diurnal warming. But before, in the next chapter, our work at the mooring sites is extended to other areas by using operational data sets.

Data are needed to initialise and force the

immediately usable for our purposes, is from the SEVIRI, AMSRE, and TMI. These instruments and what they measure are described in more detail below. To use the other data sets would require the implementation of a search algorithm to find the data at the locations required, but considerable additional computer time would be needed.

The L2P GHRSST-PP data products come with Single Sensor Error Statistics (SSES). The satellite observations used for this thesis have the GHRSST estimated bias removed. Each GHRSST observation is provided with a proximity confidence value. Only data with values considered `acceptable' and `excellent' (values 4 and 5 respectively) for the infrared observations and `acceptable' and `diurnal' (values 12 and 13 respectively) for the microwave observations are accepted for inclusion in this work. This choice selects observations far from any corrupting influences, such as cloud for infrared and rain for microwave, but keeps observations that are potentially affected by a diurnal signal.

GHRSST-PP L4 products are designed to provide the best available estimate of the SST from a combined analysis of all available SST data. In-situ data form an important component of the L4 process as these data are used to correct for biases between the satellite data sets. L4 products capitalise on the synergy benefits of using in-situ, microwave satellite SST, and infra-red satellite SST. The GHRSST L4 products include the UKMO OSTIA product described in Section 5.3.5.

For more information on the data processing specifications adopted for the GHRSST products see [33]. The three SST data products used in this chapter and the next are now introduced.

Radiometric measurements from the Spinning Enhanced Visible and Infrared Imager (SEVIRI) on-board Meteosat Second Generation (MSG) satellites (from Meteosat-8, launched August 2002, onwards) are used to derive SST observations. Imaging is achieved with a bi-dimensional Earth scan from a geostationary orbit. New images for each infrared channel are available every 15 minutes. The GHRSST product picks the `best' measurement in a 3 hour period. As an infrared measurement the images are

contaminated by cloud cover so that good

A

The Advanced Microwave Scanning Radiometer for Earth Observing Systems (AMSR-E) was launched in May 2002, aboard NASA's Aqua spacecraft which has a sun-synchronous orbit. JAXA provided AMSRE to NASA as an indispensable part of Aqua's global hydrology mission. Over the oceans, AMSRE is measuring a number of important geophysical parameters, including SST, wind speed, atmospheric water vapour, cloud water, and rain rate. A key feature of AMSRE, as with TMI is its capability to see through clouds, thereby providing an uninterrupted view of global SST and surface wind elds. It measures the temperature of the top layer of water approximately 1 mm thick, ($_{\text{subskin}}$). Missing data can be due to sun glint, rain, sea ice, and high wind speed (> 20 ms^{-1}). Error statistics are given in Table 6.1.

Match-ups	Bias (°C)	Standard Deviation (°C)	Dates
TMI { Reynolds	0.05	0.80	01/01/98 to 18/09/06
TMI { ship engine intake	−0:03	0.77	02/09/98 to 04/11/06
TMI { moored buoy	−0:08	0.57	02/09/98 to 04/11/06
TMI { drifting buoy	0:04	0.61	02/09/98 to 04/11/06
TMI { ship bucket	0.11	0.62	02/09/98 to 04/11/06
TMI { ship hull	−0:06	0.66	02/09/98 to 04/11/06
AMSRE { Reynolds	−0:05	0.76	30/05/02 to 04/11/06
AMSRE { ship engine intake	−0:01	0.75	30/05/02 to 04/11/06
AMSRE { moored buoy	−0:02	0.50	30/05/02 to 04/11/06
AMSRE { drifting buoy	−0:02	0.54	30/05/02 to 04/11/06
AMSRE { ship bucket	0:01	0.65	30/05/02 to 04/11/06
AMSRE { ship hull	−0:04	0.69	30/05/02 to 04/11/06

Table 6.1: Mean validation statistics calculated from near real time daily collocated data sets at [140].

The availability of global operational forecast and analysis data to force and initialise the model allows the freedom to run GOTM at any and many locations. An example for July 2005 in the North Atlantic is shown in Figure 6.1. Here GOTM is initialised daily at 00:00 GMT with 1

Reed parameterisation (Equation (3.5)) is used. Integrating this over a 6 hour window gives

$$\int_{T}^{T+6} I_0 dt = \int_{T}^{T+6} I_{\downarrow} (1 - 0{:}62n + 0{:}0019 \quad)(1 - \quad) \, dt; \tag{6.1}$$

where T are the 6 hourly forecast times. The left hand side of equation (6.1) is set equal to the ECMWF value, and Equation (6.1) can be rearranged to nd an e ective mean cloud value over this window,

$$n = \frac{(1 + 0{:}0019 \quad) \int_{T}^{T+6} I_{\downarrow}(1 - \quad)dt - \int_{T}^{T+6} I_0 dt}{0{:}62 \int_{T}^{T+6} I_{\downarrow}(1 - \quad)dt}{:} \tag{6.2}$$

If it is night time, so that $\int_{T}^{T+6} I_{\downarrow}(1 - \quad_0)dt = 0$, then persistence $n_k = n_{k-1}$ is assumed. A check is also made to enforce the physical cloud limits $0 \leqslant n \leqslant 1$. The net surface SWR, I_0, used in the model run is calculated using the Reed formula (3.5) with the 6 hourly cloud values derived from the 6 hourly integrated ECMWF net surface SWR as described above. The other tegrated SWR,u9.0324.08T(as)eT]-j428.9590 1.7720 Td(el)5Bj40j0 31542113 in low wind speed conditions. Thus OSTIA can b sensitive to the amount of mixing being generated in the top grid boxes and this is particularly true in low wind speed conditions. Under low wind speed conditions the surface stress is very slight and little TKE is generated, the model has a tendency to under produce TKE in such circumstances, but these values are of extreme importance when modelling the diurnal cycle. To prevent the extinguishing of TKE an internal wave parameterisation (see Section 2.3.4) can be included to represent internal wave activity which always leaves a background residue of TKE. To enhance mixing at the surface a wave breaking parameterisation (see Section 2.3.3) can be included. Under low wind stress conditions the type of surface boundary conditions (prescribed Dirichlet conditions or a ux boundary Neumann type condition) for TKE and dissipation can also make a di erence.

The starting point was to consider modelled diurnal warming estimates of over 4 °C as unlikely. The various combinations of options were tested over the selected region and chosen time period and a count was taken of the number of occurrences when the modelled diurnal warming exceeded 4 °C and a record kept of the maximum value. If the model is consistently under producing TKE at the near surface then it is expected that the number of extreme warming events will increase in number and magnitude. The modelled SST, $_{0:015m}$, is validated against cTj i(837617)12.7498consist(493)Tj d45.(67)3j1565

Mixing Options			Results		
BC	IW	WB	RMS Errors (°C)	Max DW (°C)	Extreme DW Events
Dirichlet	no	no	0.83 (0.83)	15.84 (15.82)	102 (88)
Neumann	no	no	0.84 (0.85)	19.13 (19.13)	104 (100)
Dirichlet	yes	no	0.55 (0.55)	5.09 (5.09)	33 (32)
Neumann	yes	no	0.54 (0.54)	4.97 (4.97)	21 (21)
Dirichlet	yes	yes	0.56 (0.56)	6.20 (6.20)	39 (36)
Neumann	yes	yes	0.53 (0.53)	4.94 (4.94)	15 (14)

Table 6.2: The effects of surface boundary conditions (BC), internal wave (IW), and wave breaking (WB) parameterisations on RMS differences with modelled SST at $_{0:015m}$ and SEVIRI observations, the magnitude of the maximum diurnal warming (DW) event, and the number of extreme DW events ($_{0:015m}$ > 4 °C). Values in parentheses are produced from model simulations at identical locations.

boundary conditions, but when using Dirichlet boundary conditions the wave breaking parameterisation appears to slightly heighten the occurrence of extreme warming events. In the conditions of most interest here (low wind regimes where diurnal warming [illegible]

The ECMWF predicts

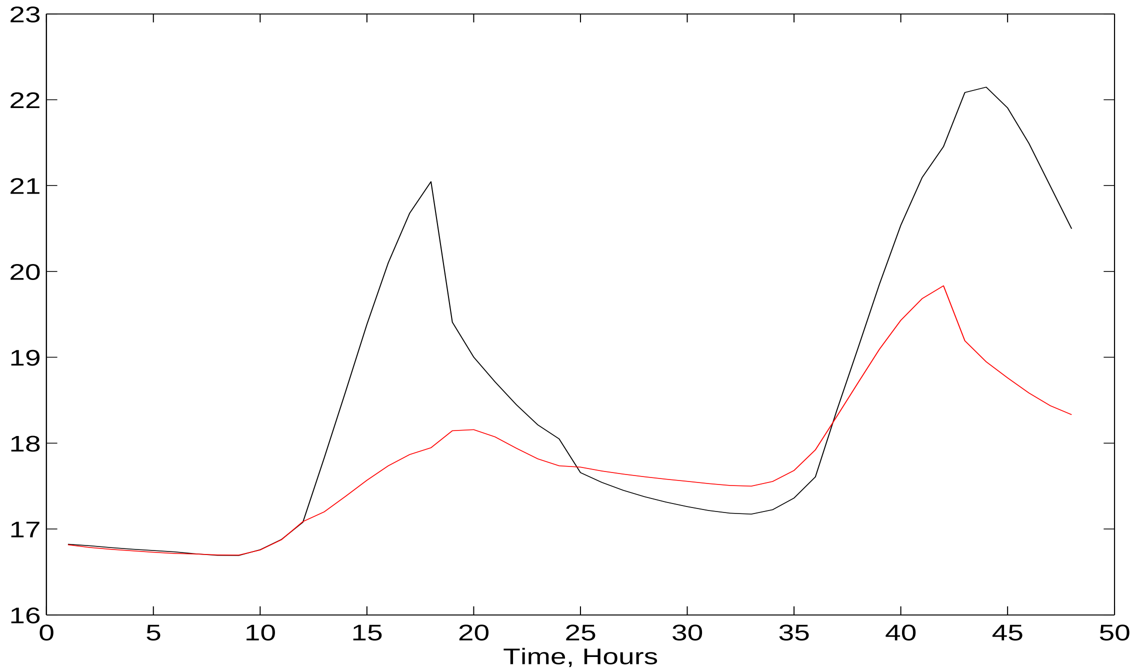

23
22
21
20
19
18
17
16
0
5
10
15
20
25
30
35
40
45
50
Time, Hours

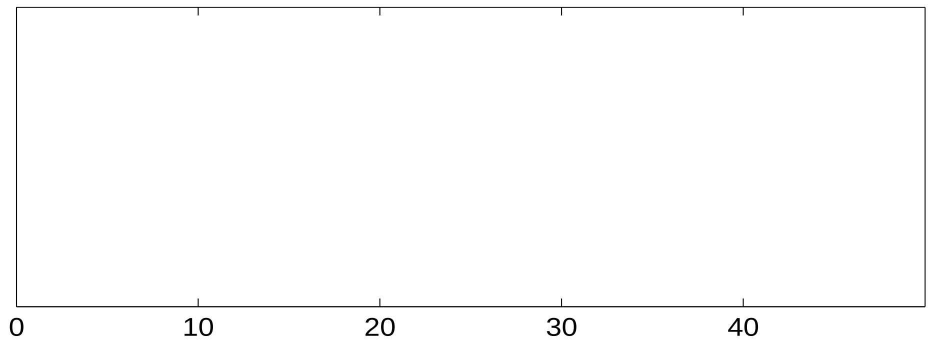
0
10
20
30
40

Having found improvements by using an IW mixing parameterisation, calculating the air-sea uxes dynamically, and implementing a better ocean radiant heating parameterisation the improved experimental set-up was implemented over the Atlantic Ocean ($-50\,^{\circ}$N to $50\,^{\circ}$N and $270\,^{\circ}$E to $359\,^{\circ}$E). Modelled diurnal variability ($_{0:015m}$) maps were produced for the rst week of January 2006 and are shown in Figures 6.4 to 6.10.

Also shown in Figures 6.4 { 6.10 for comparison are graphs of the daily modelled mean SST $\left(\overline{\ }_{0:015m}\right)$, the daily modelled mean wind stress $\left(\overline{|\tau|}\right)$, and the daily modelled peak SWR $\left(\overline{I_0}\right)$. There are not too many noticeable changes to the mean SST; however, day to day changes in the diurnal warming can clearly be seen. This particular week is during southern hemisphere summer and several places south of the equator reach a peak SWR of 1000 Wm^{-2}. (7.5 Tdi -9.7200 TD (1000)Tj 25.5199 Tj g76 -5.039 0.6637 0 k)Tj 2

Figure 6.4: A map of the A

Figure 6.5: A map of the Atlantic Ocean showing daily mean SST (

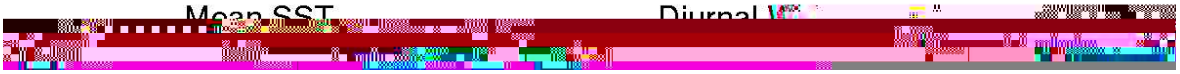
Mean SST
Diurnal

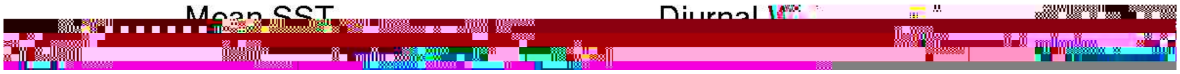
Mean SST
Diurnal

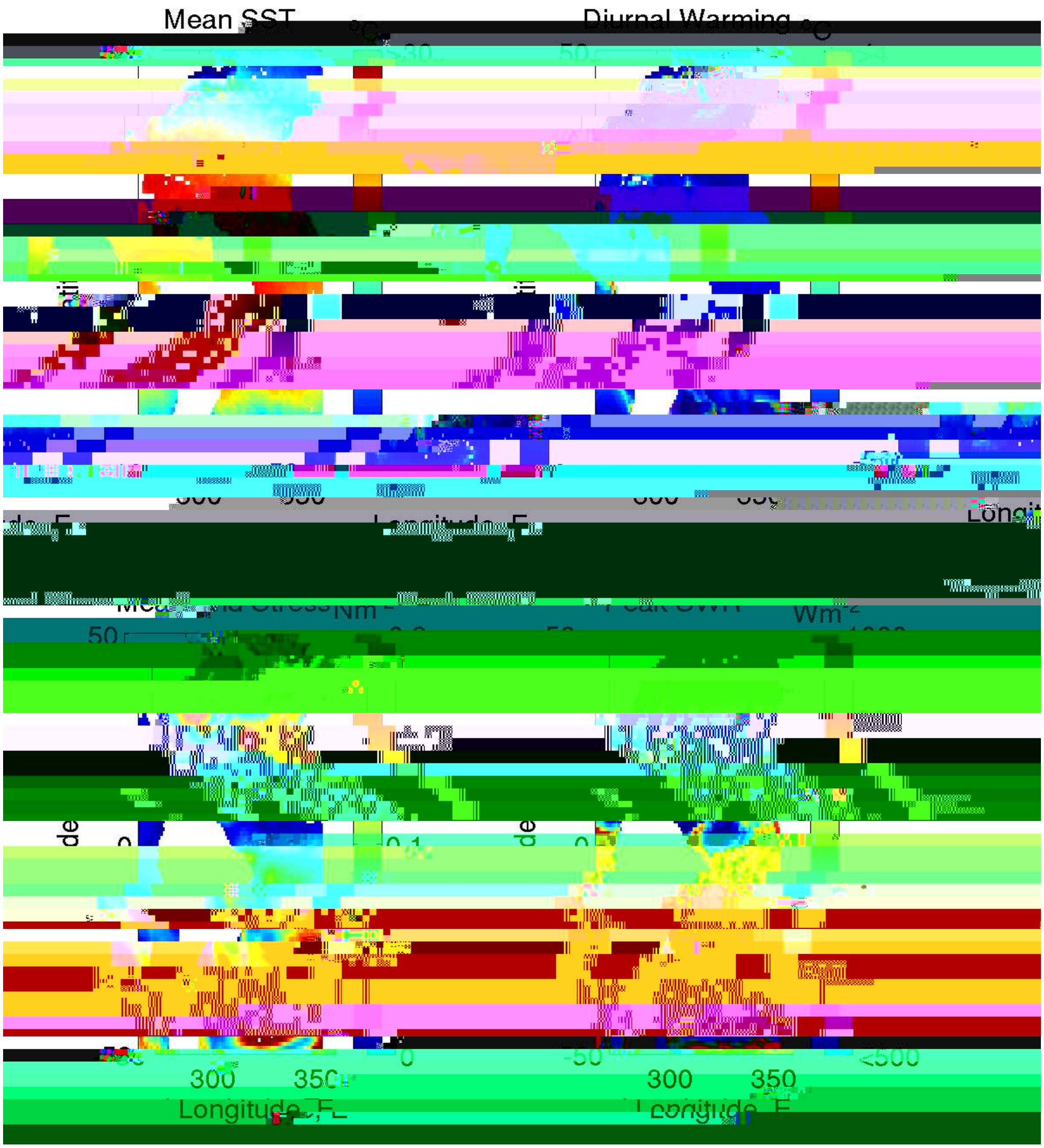

Figure 6.7: A map of the Atlantic Ocean showing daily mean SST $\left(\overline{\ }_{\mathbf{0:015}m}\right)$, diurnal warming ($_{\mathbf{0:015}m}$), daily mean wind stress $\left(\overline{|\tau|}\right)$, and daily peak SWR $\left(\overline{\mathbf{I_0}}\right)$ for the 4^{th} January 2006.

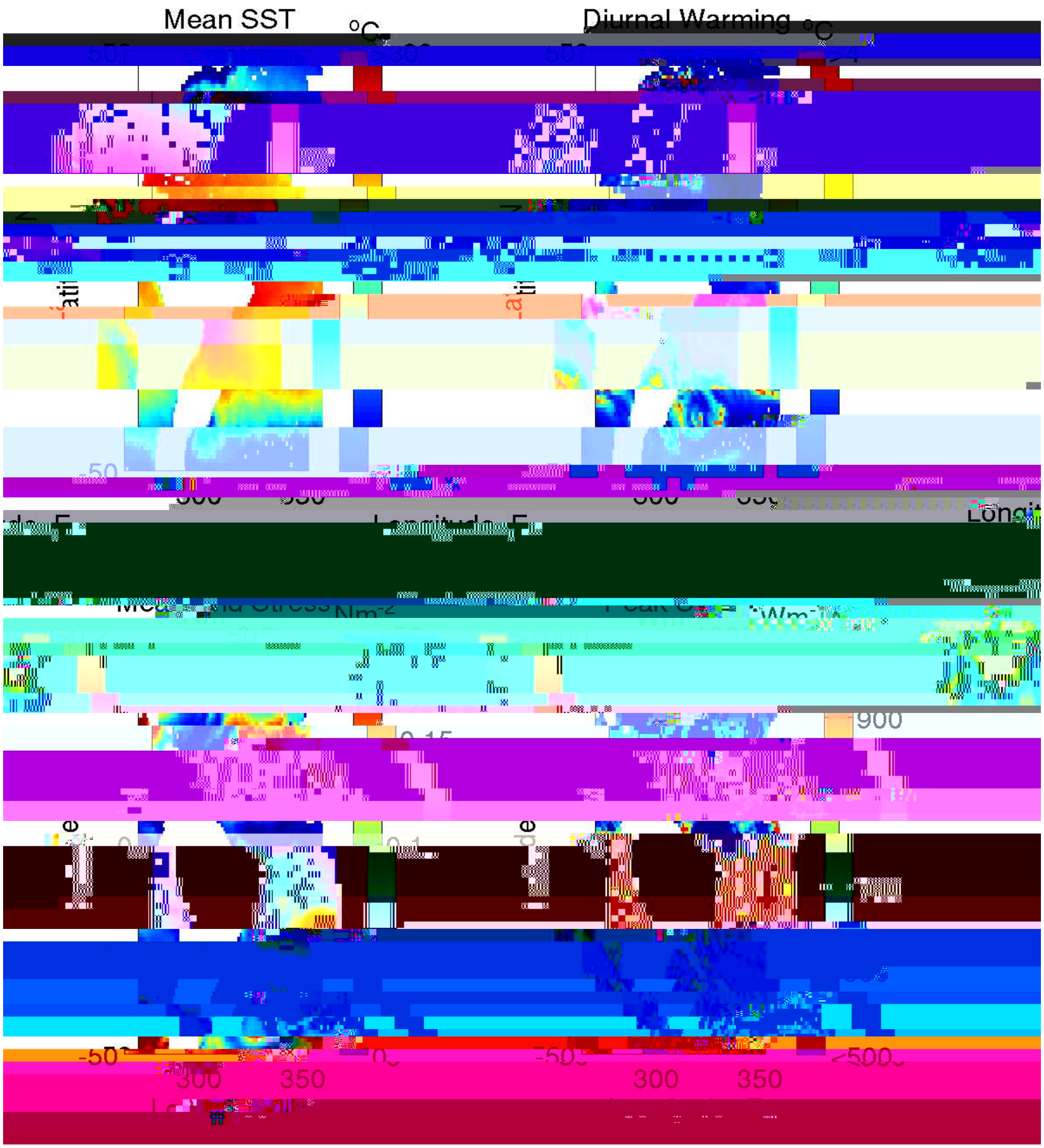

Figure 6.8: A map of the Atlantic Ocean showing daily mean SST ($\overline{\ }_{0:015m}$), diurnal warming ($_{0:015m}$)015

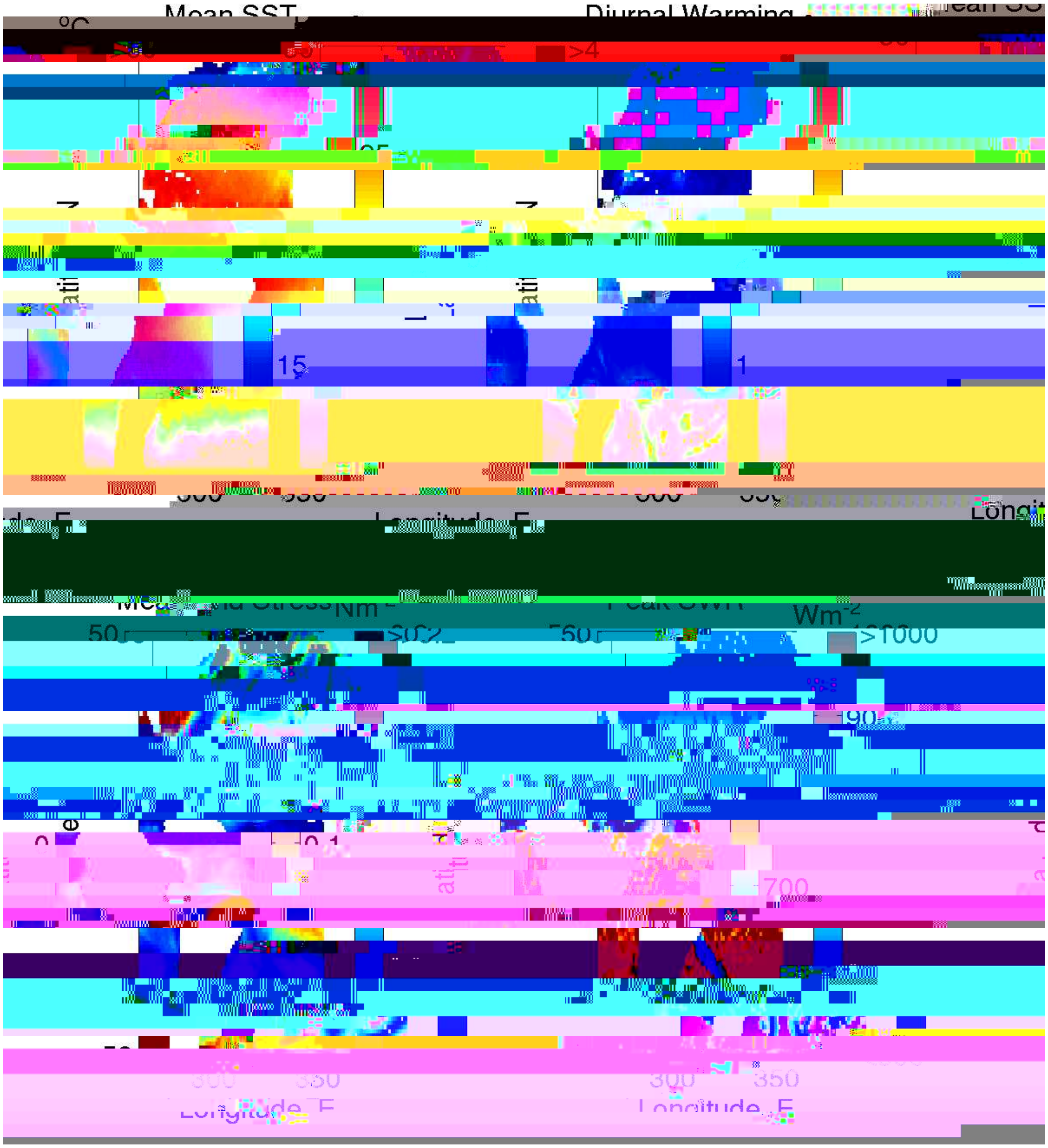

Figure 6.9: A map ofof Fi1997635h 35 1ET 6.6758.899.24-0 T4 949.08 17m /0767 DBI /IM true /V

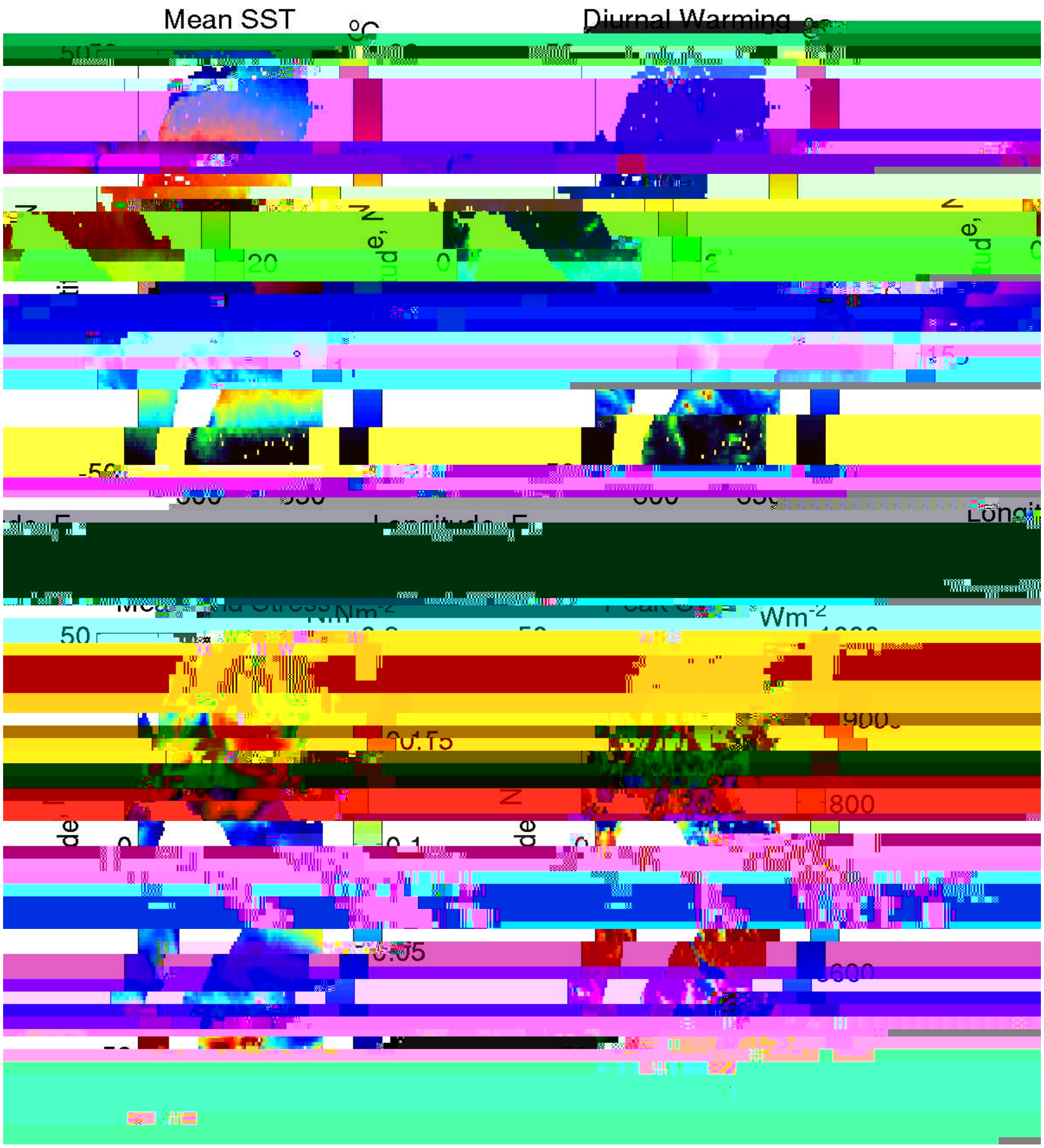

Figure 6.10: A map of the Atlantic Ocean showing daily mean SST $\left(^{-}_{0:015m}\right)$, diurnal warming ($_{0:015m}$), daily mean wind stress $\left(\overline{|\tau|}\right)$, and daily peak SWR $\left(\overline{I}\right.$

over 6 particular years does show some similarities - particularly the susceptibility of the latitude band $-40\,^{\circ}$N to $-20\,^{\circ}$N to strong diurnal warming. As far as is known plots such as Figures 6.4 { 6.10 are a rst attempt to produce such maps based on model output and are of added value in several respects. Firstly they can be produced globally complete on a daily basis, as they do not rely on particular overpass paths and times or the availability of day/night overlaps in the observations. Secondly many climate and ocean modellers are reluctant to include a diurnal cycle in their models because of the increased cost of extra vertical resolution; therefore the satellite community are required to provide observations for assimilation that are not `corrupted' by a diurnal signal. These maps can be used to highlight areas where observations are likely to have a diurnal warming signal and ag observations in the vicinity; or better still use the model output to remove the diurnal bias at any location. Thirdly this simple model approach could potentially be useful for improving accuracy in observational foundation SST products by again removing the diurnal signal and reducing bias. It follows from the previous two points that what is actually required is not necessarily a diurnal warming value but the skin to bulk measure at an observation time. For example, a satellite measures the temperature at the skin or sub-skin depth and a quanti cation of the near surface variability is needed to convert this measurement to the foundation depth for inclusion in a bulk SST product,

OSTIA on average. This should be expected as OSTIA represents a night time or foundation temperature, whereas the match-ups here compare all observations, including those that contain a diurnal signal. It is odd, however, that the daytime AMSRE and TMI observations show a positive bias (OSTIA warmer than

time.

In the next chapter a method is developed by which the modelled diurnal warming estimates are improved by the assimilation of satellite observations of SST. In combining model output with observations over the diurnal cycle uncertainties in the original modelled output are reduced.

Chapter 7

Assimilating Satellite SST Observations into the Diurnal Cycle

n c n

The work in Chapter 6 demonstrated how operational forecast data can be used to force a collection of mixed layer models in order to estimate diurnal variability. The output from these model simulations can be used to evaluate diurnal warming patterns in time and over a wide area, as seen in Figures 6.4 { 6.10. In the introduction to Chapter 5 it was described how data assimilation is used to merge dynamical

cloud cover. In this chapter

provide the diurnal warming estimate at the observation time. This observation operator can not be invariant as the transformation will depend on the particular local conditions at a given time. Developing such an operator is not an easy task; several attempts at parameterising the likely warming (e.g. [151], [68], [42], and [137]) have experienced di culties in representing the full range of outcomes in this highly complex and non-linear system. A prognostic skin SST scheme has been tried with the ECMWF atmospheric model [158]; however, its e ect on weather forecasting and four-dimensional data assimilation have yet to be fully examined. In Chapters 4 and 6 of this thesis results are presented which show some degree of success in modelling the diurnal variability. The use of GOTM in this way can be viewed as providing a dynamic observation operator H, because by modelling the diurnal cycle and providing good near surface resolution we are able to quantify the transform from foundation temperature to skin or sub-skin temperature. However the modelled diurnal variability is not without error. This error could be reduced by assimilating the observations into the diurnal cycle at the correct time and near surface depth. How this should best be done is an interesting problem in itself.

The extent of diurnal warming is predominately dependent on two key factors: sea surface wind speeds and the strength of the insolation, whose variance at a given location and time is largely determined by the cloud cover. As explained in Section 1.5 strong insolation during daytime, under clear skies, causes a warm stable strati ed layer to appear, but this near surface warming can easily be broken down in the presence of wind driven mixing. The uncertainties in these forcing variables (cloud cover and wind speed) thus contribute to the uncertainty in the modelled diurnal warming estimates. Unfortunately in NWP there is not a single, simple law which governs the formation of cloud and thus it is very di cult to parameterise and is a vational comparisons are di cult and errors vary for di erent regions and time scales [17]. In diurnal cycle modelling the high values are not of concern as no diurnal signal forms at high wind speeds; howev [illegible]

O e e

A forcing parameter pair ($_{A}$; $_{B}$) associated with adjustments to the wind speed, w, and cloud cover, n, is introduced and its value tuned over each 24 hour window. Five model realisations are required over the time window. To start with, the parameters are set at zero and the wind speeds and cloud cover values are derived from ECMWF 6 hourly forecasts. A further model run is performed in which $_{B}$ is perturbed. The results of these simulations are use9.4322tTj 1Tj 201.8747 0 Tdffl6s9c3 0 0 Td 50w.

because of the strong cloud limits, see Equations (7.10) and (7.11). The SST can now be viewed as a function of the parameters

$$ {}_{150} = {}_{150}({}_{A} ; {}_{B}) : \qquad (7.7) $$

The observed forcing data, n_{obs}, is obtained by using the 6 hourly integrated ECMWF quadrants:

$$
\begin{aligned}
0 < {}_A &\leq 1; \\
0 < {}_B &< 3;
\end{aligned}
\tag{7.10}
$$

if $J_0 > 0$ and

$$
\begin{aligned}
-1 \leq {}_A &< 0; \\
-1 < {}_B &< 0;
\end{aligned}
\tag{7.11}
$$

if $J_0 < 0$. In the trivial case where $J_0 = 0$ the optimal parameters are $(0; 0)$. The choice of parameter range is (where possible) based on physical assumptions. The range for ${}_A$ is therefore the maximum and representing a 25% change in the wind speed forcing. The cost function $J(0;\ _B)$ is evaluated over the period. Then estimate the sensitivity or local gradient of J_0 with respect to $\ _B$,

$$\frac{\partial J_0}{\partial \ _B} \quad \frac{J(0;\ _B) - J_0}{\ _B}: \tag{7.14}$$

STEP 3

Assuming the cost function $J(0;\ _B)$ varies linearly within the feasible $\ _B$ parameter range (Equation (7.10) or (7.11)) we are able to construct the line

$$J(0;\ _B) = \frac{\partial J_0}{\partial \ _B}\ _B + J_0 \tag{7.15}$$

and determine an `optimal' value

$$\ ^*_B = \left(\frac{\partial J_0}{\partial \ _B}\right)^{-1}\left(\min_{\text{feasible}\ _B} |J(0;\ _B)| - J_0\right): \tag{7.16}$$

The aim is to choose $J(0;\ _B)$ as small as possible without taking the line, Equation (7.15), outside the feasible limits set in Equation (7.10) or (7.11). This is calculated through an iterative process:

$$\ ^k_B = \left(\frac{\partial J_0}{\partial \ _B}\right)^{-1}\left(J(0;\ _B)^k - J_0\right); \tag{7.17}$$

where $k = 1; \ldots; end$ are the iterates. If $J_0 > 0$ then

$$J(0;\ _B)^k = J_0 - \ \ k \tag{7.18}$$

and if $J_0 < 0$ then

$$J(0;\ _B)^k = J_0 + \ \ k; \tag{7.19}$$

where the step size for J, , is chosen as $0{:}05\,^\circ$C. This allows $J(0;\ _B)^k$ to be evaluated to within $0{:}05\,^\circ$C. At each iteration $\ ^k_B$ (Equation (7.17)) is determined and a calculation made to ascertain whether this value lies outside the feasible range, Equations (7.10) or (7.11). The iteration loop ends when $J(0;\ _B)$ reaches zero, or alternatively when $\ ^k_B$ no longer

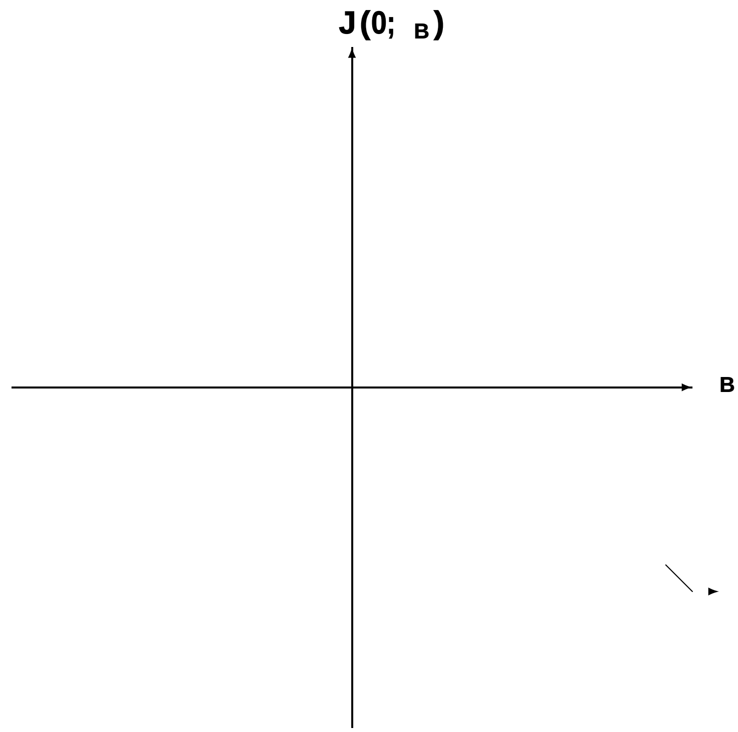
J(0; B)
B

The assumption in this method is that J varies linearly with respect to the parameters $(_A; \ _B)$ within the feasible limits. The validity of this assumption is very di cult to test thoroughly because of the cost function, Equation (5.3) in Section 5.2. Minimising this produces the maximum likelihood estimate which for random, unbiased, Gaussian observations is a minimum variance estimate. For this particular problem the cost function could be adapted to include the constraints. For example

$$J(\ _A;\ _B) = \sum_{i=1}^{N} \frac{1}{\ _i^2} \left(\ _i - \ _i^{obs}\right)^2$$

$$- \quad {}^{A}\ [\log(\ _A + 1)\ 1)$$

1. **Control**

   Step 1 only, the parameters, $_A$ and $_B$, are set to zero.

2. **Wind Only**

   Here only the wind value is corrected thus only the parameter $_B$ is tuned. Therefore step 4 is not required.

3. **Cloud Only**

   As above except cloud cover rather than wind speed is corrected.

4. **Wind then Cloud**

   The wind speed value is corrected rst followed the cloud value as originally described.

5. **Cloud then Wind**

   As above except the cloud cover correction is determined rst followed by the wind speed correction.

6. **Wind and Cloud**

   In this approach the wind and cloud parameters are determined together. To nd an `optimal' parameter pair a rst order Taylor expansion of two variables is used

$$J(\,_A + \,_A;\,_B + \,_B) = J(\,_A;\,_B) + \,_A\frac{\partial J(\,_A;\,_B)}{\partial\,_A} + \,_B\frac{\partial J(\,_A;\,_B)}{\partial\,_B}. \quad (7.22)$$

By choosing $(\,_A;\,_B) = (0;0)$ and $(\,_A;\,_B) = (\,_A;\,_B)$, and denoting $S_A = \frac{\partial J}{\partial\,_A}$ and $S_B = \frac{\partial J}{\partial\,_B}$, Equation (7.22) can be rearranged as

$$_B = -\frac{S_A}{S_B}\,_A + \frac{J - J_0}{S_B}. \quad (7.23)$$

This is an equation of a straight line in parameter space $(\,_A;\,_B)$. If a value for $J = J(\,_A;\,_B)$ is chosen such that $0 \leq |J| \leq |J_0|$ then an equation in two unknowns ($_A$ and $_B$) results, reducing the problem to two degrees of freedom. As before an iteration reduces J and checks whether the line, Equation (7.23), falls within the trust region. When J reaches zero or the line moves outside the trust region the optimal parameters, $(\overset{*}{A}; \overset{*}{B})$, are then chosen as the mid-point of the line, Equation (7.23), within the trust region, Equation (7.10) or (7.11). This is shown in Figure 7.3.

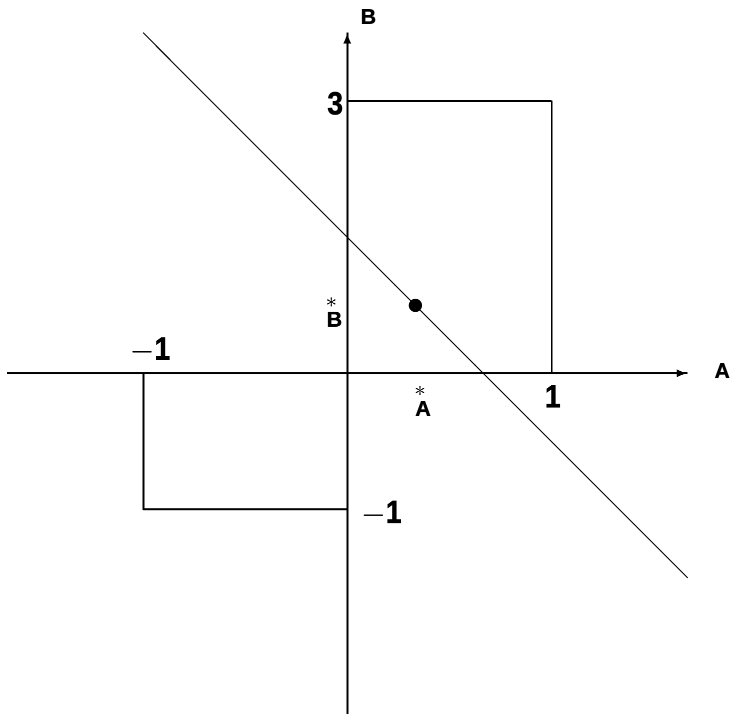

	Mean	RMS	STD
Control	0.02 (0.02)	0.55 (0.57)	0.55 (0.55)
Cloud Only	−0:16 (−0:16)	0.47 (0.47)	0.44 (0.44)
Wind Only	0.01 (0.01)	0.42 (0.42)	0.42 (0.42)
Cloud then Wind	−0:02 (−0:02)	0.39 (0.39)	0.39 (0.39)
Wind then Cloud	−0:06 (−0:06)	0.36 (0.36)	0.36 (0.36)
Wind and Cloud	−0:02 (−0:02)	0.40 (0.40)	0.40 (0.40)

Table 7.1: Results showing the mean, RMS, and STD of $_{0:015m} - {}_{SEVIRI}$, in °C, for the area −45°N to −25°N and 300°E to 330°E during 1^{st}{7^{th} January 2006. The numbers in parenthesis compare only those results calculated at locations and days simulated in each case.

sensitivity to changes in wind than changes in the cloud cover. For example, if the cloud correction is made rst then the smaller sensitivity will lead to unreasonably large changes in cloud cover to provide the SST change, whereas if the cloud correction is made after a wind correction then the remaining change needed in modelled SST is much smaller and so the less sensitive cloud cover parameter is suitable. The most e ective method is to tune rst the [illegible] evaluating model-observation differences using IR measurements, the comparison is to the parameterised modelled skin temperature (see Section 3.5.9) whereas for the MW measurements the comparison is with the top modelled SST, at a depth of $0.015\,\mathrm{m}$, without the cool skin effect. Results from this improved method are presented in Table 7.2. Model output is compared separately to IR observations only and combined IR and MW observations. The control simulation makes no corrections to the forcing were necessary. If the SST observations are then used to adjust the wind forcing then the errors are significantly reduced with the RMS differences falling to $0{:}34\,^{\circ}$C in the IR case and $0{:}53\,^{\circ}$C in the IR and MW case. This is further reduced when a correction is made to cloud cover values at occasions when only MW observations are present. The resulting model-observation differences after assimilation may now be approaching

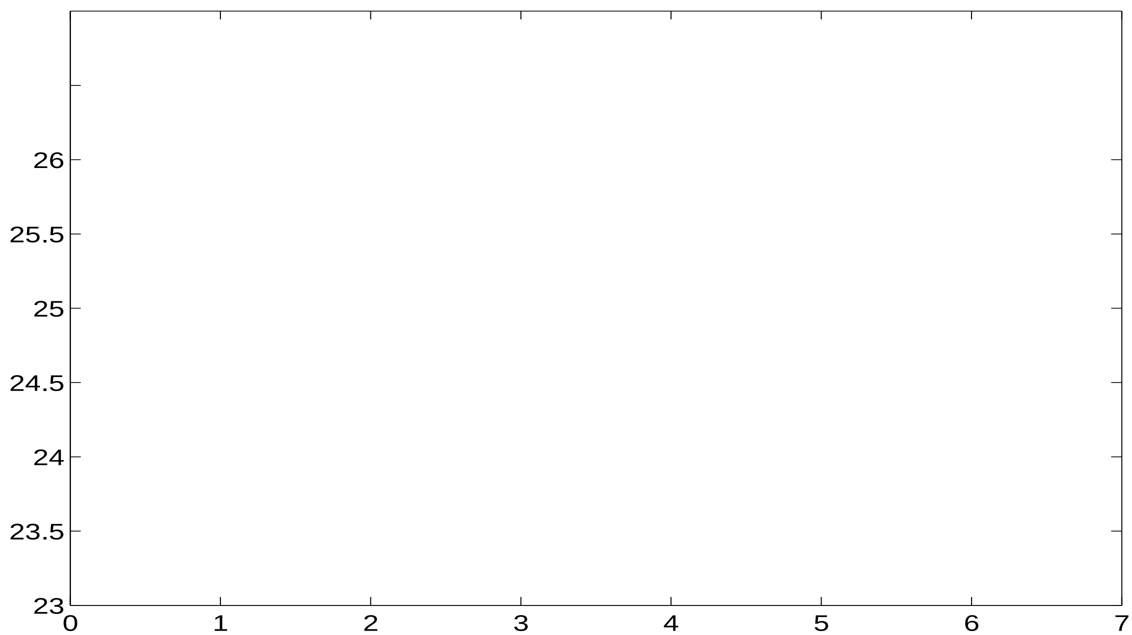

26
25.5
25
24.5
24
23.5
23
0
1
2
3
4
5
6
7

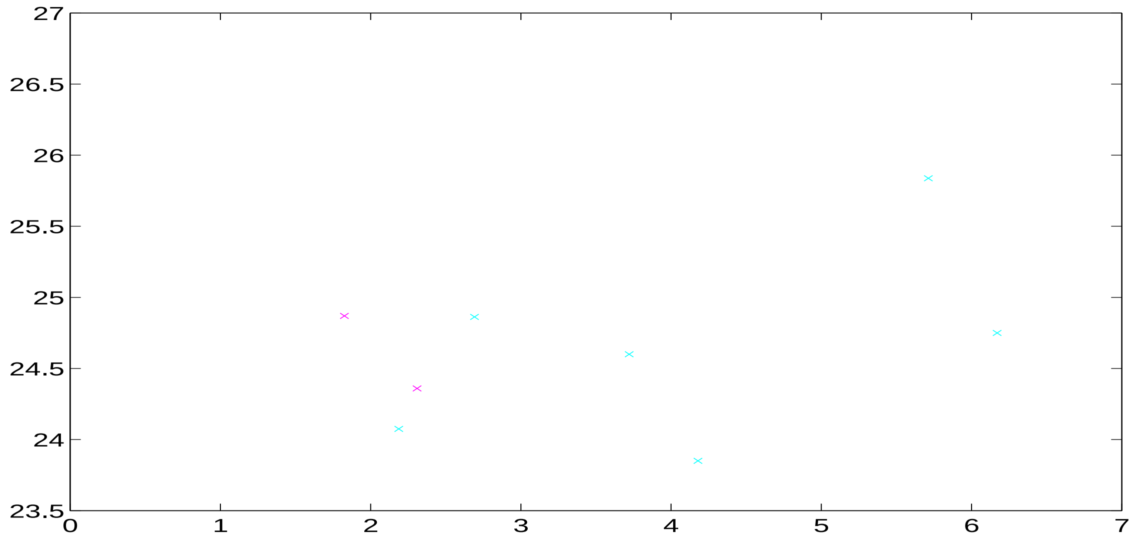

27
26.5
26
25.5
25
24.5
24
23.5
0
1
2
3
4
5
6
7

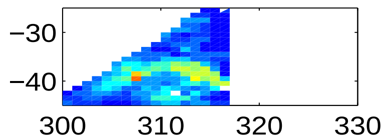

−30
−40
300
310
320
330

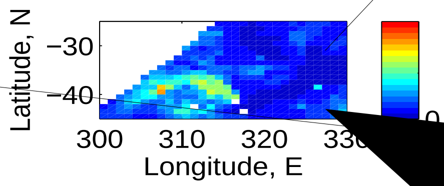
Latitude, N
−30
−40
300
310
320
Longitude, E

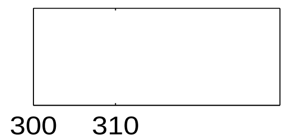
300
310

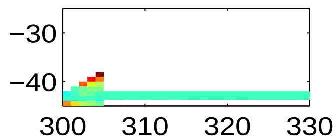

−30
−40
300
310
320
330

	No. Obs.	Mean	RMS	STD
SEVIRI only	2343	$-0{:}25$	0.62	0.57
AMSRE only	2220	0.20	0.80	0.77
TMI only	1532	0.37	0.98	0.91

Table 7.3: Results showing the number of observations, the mean, RMS, and STD of $_{control} - \ _{obs}$, in $^{\circ}$C, for individual satellite types. For the area -45°N to -25°N and 300°E to 330°E during 1st{7th January 2006.

the AMSRE and TMI observations are cooler on average than the modelled SST. This suggests that the observations have some systematic errors in this area at this time, with SEVIRI SST systematically too warm and/or AMSRE and TMI observations systematically too cool. The model could also have a warm bias and be estimating too great a cool skin correction. This seems unlikely as the parameterised cool skin correction for this period was on average 0:15°C, i.e. smaller than the SEVIRI only mean di erence. The model simulations are dependent on the OSTIA SST at the start of each day; therefore any errors in OSTIA will also be apparent (see Section 7.4.6). The RMS v82002 Td 06.

	No. Obs.	Mean	RMS	STD
daytime	2799	0.14	0.53	0.51
night time	1365	0.00	0.50	0.50

Table 7.4: Results showing the number of observations, the mean, RMS, and STD of $_{analysis} - \ _{obs}$, in $^{\circ}$C, during daytime (10{16) and night time (22{04) local time. For the area -45°N to -25°N and 300°E to 330°E during 1st{7th January 2006.

C s s O A

To further determine whether the biases are due to model or observations the individual satellite observations were also compared to the OSTIA value.

	No. Obs.	Mean	RMS	STD
SEVIRI only	2525	$-$0:22	0.56	0.51
AMSRE only	2256	$-$0:08	0.70	0.69
TMI only	1532	$-$0:20	0.87	0.84
all obs	6333	$-$0:17	0.69	0.67
daytime SEVIRI only	721	$-$0:51	0.76	0.56
daytime AMSRE only	1249	$-$0:29	0.77	0.71
daytime TMI only	1345	$-$0:22	0.89	0.86
daytime all obs	3315	$-$0:31		

est RMS di erence of the three instruments when compared to OSTIA. The biases are all negative for daytime observations and all positive for night time observations. However, the daytime biases are larger and when comparing all 6333 observations a bias of $-0{:}17\,^{\circ}$C is found. Indicating the satellite observations on average are warmer than OSTIA. The sharp di erence in day and night time mean values demonstrates the presence of diurnal signals in the daytime observations. OSTIA is the mean value of these observations, as well as others, and after the assimilation. These results are presented in Table 7.6.

	No. Obs.	Mean	RMS	STD
ECMWF-AMSRE	2009 (1635)	$-$0:07 ($-$0:12)	1.76 (1.72)	1.76 (1.71)
ASSIM-AMSRE	1635	$-$0:23	2.74	2.73
ECMWF-TMI	1278 (1212)	$-$0:49 ($-$0:49)	1.68 (1.60)	1.61 (1.52)
ASSIM-TMI	1212	$-$0:45	2.57	2.53
ECMWF-ALL	3287 (2847)	$-$0:23 ($-$0:28)	1.73 (1.67)	1.71 (1.64)
assim-ALL	2847	$-$0:33	2.67	2.65

Table 7.6: Results comparing the ECMWF forecast wind speeds before and after assimilation to the AMSRE and TMI wind measurements showing the number of observations, the mean, the RMS, and STD di erences in ms^{-2}. For the area $-45\,^{\circ}$N to $-25\,^{\circ}$N and 300 $^{\circ}$E to 330 $^{\circ}$E during 1st{7th January 2006. The numbers in parenthesis are calculations only at the locations and times when wind speeds are corrected in the assimilation.

The results in Table 7.6 reveal that the satellite measured winds, particularly from TMI, are slightly stronger than the ECMWF forecasted values. The RMS di erences between the ECMWF winds and all the satellite derived winds is 1:73 ms^{-1}. After the ECMWF winds have been corrected in the assimilation process the RMS is approximately increased by 1 ms^{-1} in all cases. However the resulting error is just outside the quoted mission accuracy of the AMSRE product (1 ms^{-1}) [79], although validation against buoy and scatterometer data at very low wind speeds is particularly di cult [79].

In this chapter a data assimilation method has been developed that assimilates satellite derived SST observations into a diurnal cycle model. It is proposed that model errors in diurnal warming estimates are primarily caused by uncertainties in NWP forcing data. Other sources of errors, such as errors in model parameterisations and incorrect vertical

Chapter 8

Conclusions

Accurate knowledge of SST is extremely important for ocean and atmospheric sciences, perhaps most crucially for its central role in air-sea ux calculations. The diurnal cycle is a fundamental mode of the climate system and much evidence is presented in Chapter 1 to show how the diurnal variability of SST has impacts on longer timescales. Awareness of the diurnal cycle is also shown diurnal details of the mixing scheme are documented.

Diurnal stratification is driven by solar radiative warming of the upper ocean. The penetration of SWR into the ocean is an important concept for diurnal cycle modelling. Many parameterisations exist that attempt to resolve the amount of ocean radiant heating at depth; these are outlined in Chapter 3. However only the most advanced methods should be used for modelling the diurnal cycle as it is important to resolve solar transmission variations within the upper few metres. The parameterisation of air-sea fluxes are also extremely important for accurately modelling diurnal variability. The ability to measure air-sea fluxes is limited; therefore their calculation is dependent on parameterisations using commonly available meteorological data. In Chapter 3 a derivation of air-sea flux formulae is given followed by a description of the two algorithms tested in Chapter 4, of which the TOGA COARE method developed by Fairall et al produced the best results.

In Chapter 4 the model was tested at three mooring sites in different parts of the world. Various aspects of upper ocean variability were examined. The model was shown to have very good accuracy in estimating SSTs over the observed time-series. The k[illegible] the SST assimilation problem were experimented with at the mooring sites. One such scheme assimilated the SST increment by correcting all temperatures within the mixed layer. More novel approaches were also explored involving the use of an SST observation to estimate a cloud cover value. However, it was often di cult to attribute an SST error to a particular cause. A discussion was also presented on the possible use of comparing modelled and observed changes in SST to determine errors in the modelled mixed layer depth.

The use of the 1-D model is extended by utilising operational forecast and analysis data sets to initialise and force the simulations. Details are given on how the 6 hourly resolution of the meteorological data can beed can lead to errors in modelled diurnal warming estimates as a result of incorrect wind speed and cloud cover values. A new method is developed in Chapter 7 that uses the SST observations to derive corrections, within uncertainty bounds, to wind speed and cloud cover values. This is the rst time SST data has been assimilated into a diurnal cycle model. Adjusting the forcing to be more consistent with the SST observations is an original approach to the problem. Results are presented which show improvements when using this assimilation algorithm. It is also demonstrated how the method could be implemented on a global scale.

M n n ng

This thesis opened with (/Tj(b)Tj/F2 1 Tf 2.2 2 Tf (Tar nming) Tj opics1 0 Td 697is models were run over a wide range of locations and the results used to produce daily spatial maps of the diurnal warming signal in SST. This mesh of models forced with the ubiquitous NWP data has the potential to become a very useful method, viz, in identifying areas of diurnal warming and quantifying diurnal signals in observational SST data.

A O se O e e e e ed

This thesis has highlighted the depth disparity between SST observations and their model counterparts as well as the lack of model representation of diurnal variability seen in observations. In order to reduce errors in an assimilation procedure an observation operator is needed to transform model variables of bulk temperatures into the skin and sub-skin temperatures of satellite derived SSTs. The reverse is true for producing foundation SST observational products; for this case SST observations `corrupted' by a signal need to be converted to the base temperature from which the diurnal thermocline has developed. It is demonstrated how a 1-D model equipped with ne near surface resolution and diurnal forcing, as used in this thesis, is an e ective dynamic observation operator for the uses outlined here.

Ad e e Ass

A literature review of SST data assimilation techniques carried out in Chapter 5 highlights several shortcomings in current schemes. These include the absence of an observation operator to account for diurnal signals, instabilities and disruptions caused by adjusting prognostic variables, a lack of vertical correlations due to a dearth of vertical model resolution and uncertainty of how information content at the surface can inform the sub-surface, and an imbalance between thermal and dynamical elds which reduces the e ectiveness of the assimilation.

The model used in this thesis can be viewed and applied as an observation operator in the data assimilation process, as indicated in the previous section. The model attempts to resolve observable scales and therefore A0.038dpp.5094 0 Td (balance) into the diurnal cycle. It is shown how perfect correlations within the mixed layer can be assumed so that night time SST observations can be used to adjust all ocean temperatures in the mixed layer. To reduce the original cause of SST errors attempts were made to account for SST errors by using SST observations to estimate cloud cover values. It is also shown how a comparison between changes in modelled and observed SST could be used to correct mixed layer depths diagnosed by the model. A new and novel

3

In answering the aims set out in Chapter 1

et al [91] used the parameterisation of Stuart-Menteth et al [137] in an attempt to remove diurnal warm la

agnostics of interest would include comparing the mixed layer depths as estimated by FOAM and GOTM.

The work carried out in this thesis could certainly form the basis of a more comprehensive system that could be developed for an operational centre pro

Bibliography

[1] J.Icarus Allen, J. R. Siddorn, J. C. Blackford, and F. J. Gilbert. Turbulence as a control on the microbial loop in a temperate seasonally strati ed marine systems model. J. Sea Res., 52:1{20, 2004.

[2] S. P. Anderson and R. A. Weller. Surface buoyancy forcing and the mixed layer of the western Paci c warm pool: Observations and 1d model results. J. Climate, 9:3056{3085, 1996.

[3] I. Andreu-Burillo, J. Holt, R. Proctor, J. D. Annan, I. D. James, and D. Prandle. Assimilation of sea surface temperature in the POL coastal ocean modelling system. J. Mar. Syst., 65:27{40, 2007.

[4] J. D. Annan and J. C. Hargreaves. Sea surface temperature assimilation for a three-dimensional baroclinic model of shelf seas. Cont. Shelf Res., 19:1507{1520, ol72nce3Tj (nd)Tj 22.6694 0 Td grea,ion1.mixed

[17] D. B. Chelton and M. H. Freilich. Scatterometer-based assessment of 10-m wind analyses from the operational ECMWF and NCEP numerical weather prediction models. Mon. Wea. Rev., 133:409{429, 2005.

[18] D. Chen, S. E. Zebiak, and M. A. Cane. Initialization and predictability of a coupled ENSO forecast model. Mon. Wea. Rev., 125:773{788, 1997.

[19] R. M. Clancy, J. M. Harding, K. D. Pollak, and P. May. Quanti cation of improvements in an operational global-scale ocean thermal analysis system. J. Atmos. Oceanic Technol., 9:55{65, 1992.

[20] R. M. Clancy, P. A. Phoebus, and K. D. Pollak. An operational global-scale ocean thermal analysis system. J. Atmos. Oceanic Technol., 7:233{254, 1990.

[21] N. E. Clark, L. Eber, R. M. Laurs, J. A. Renner, and J. F. T. Saur. Heat exchange between ocean and atmosphere in the eastern north Paci c for 1961-1971. Technical report, NOAA, 1974.

[22] M. C. Cooper and K. Haines. Data assimilation with water property conservation. J. Geophys. Res., 101:1059{1077, 1996.

[23] P. Cornillon and L. Stramma. The distribution of diurnal sea surface warming events in the western Sargasso Sea. J. Geophys. Res., 90:11811{11815, 1985.

[24] P. D. Craig and M. L. Banner. Modeling wave-enhanced turbulence in the ocean surface layer. J. Phys. Oceanogr., 24:2546{2559, 1994.

[25] J. Crank and P. Nicolson. A practical method for numerical evaluation of solutions of partial di erential equations of the heat-conduction type. Proc. Cambridge Philos. Soc., 43:50{67, 1947.

[26] G. Danabasoglu, W. G. Large, J. J. Tribbia, P. R. Gent, and B. P. Briegleb. Diurnal coupling in the tropical oceans of CCSM3. J. Climate, 19:2347{2365, 2006.

[27]

[37] C. W. Fairall, E. F. Bradley, D. P. Rogers, J. B. Edson, and G. S. Young. Bulk parameterization of air-sea uxes for

[46] N. I. M. Gould and S. Ley er. An introduction to algorithms for nonlinear optimization. Technical Report 031, RAL, 2002.

[47] W. J. Gould and J. Turton. Argo - sounding the oceans. Weather, 61:17{21, 2006.

[48] A. K. Gri th and N. K. Nichols. Adjoint techniques in data assimilation for estimating model error.

[55] H. J. Isemer, J. Willebrand, and L. Hasse. Fine adjustment of large scale air-sea ux parameterizations b

[65] K. B. Katsaros. Parameterization schemes and models for estimating the surface radiation budget. In G. L. geernaert and W. J. Plant, editors, Surface Waves and Fluxes, volume II, pages 339{368. Kluwer, 1990.

[66] K. B. Katsaros and A. V. Soloviev. Vanishing horizontal sea surface temperature gradients at low wind speeds. Bound. Layer Met., 112:381{396, 2004.

[67] K. B. Katsaros, A. V. Soloviev, R. H. Weisberg, and M. E. Luther. Reduced horizontal sea surface temperature gradients under conditions of clear skies and weak winds. Bound. Layer Met., 116:175{185, 2005.

[68] Y. Kawai and H. Kawamura. Evaluation of the diurnal warming of sea surface temperature using satellite-derived marine meteorological data. J. Oceanogr., 58:805{814, 2002.

[69] P. D. Killworth, D. A. Smeed, and A. J. G. Nurser. The e ects on ocean models of relaxation toward observations at the surface. J. Phys. Oceanogr., 30:160{174, 2000.

[70] S. Kizu. Systematic errors in estimation of insolation by empirical formulas. J. Oceanogr., 54:165{177, 1998.

[71] J. Kondo. Air-sea bulk transfer coe cients in diabatic conditions. Bound. Layer Met., 9:91{112, 1975.

[72] E. Kraus and S. Turner. A one-dimensional model of the seasonal thermocline: The general theory and its consequences. Tellus, 19:98{106, 1967.

[73] E. B. Kraus and J. A. Businger. Atmospheric-Ocean Interaction. Oxford University Press, 1994.
5)Tj /R274167 0 Td T(consequences.)Tj /5Td 5

[75] D. V. Ledvina, G. S. Young, R. A. Miller, and C. W. Fairall. The e ects of averaging on bulk estimates of heat and momentum uxes for the tropical western Paci c ocean. J. Geophys. Res., 98:20211{20218, 1993.

[76] T. W. Liu, K. B. Katsaros, and J. A. Businger. Bulk parameterization of air-sea exchanges of heat and water vapor including the molecular constraints at the interface. J. Atmos. Sci., 36:1722{1735, 1979.

[77] J. Lu and W. W. Hsieh. On determining initial conditions and parameters in a simple coupled atmosphere-ocean model by adjoint data assimilation. Tellus, 50a:534{544, 1998.

[78] A. Manda, N. Hirose, and T. Yanagi. Feasible method for the assimilation of satellite-derived SST with an ocean circulation model. J. Atmos. OcSST

[85] General Ocean Turbulence Model. http://www.gotm.net, April 2007.

[86] General Ocean Turbulence Model. http://www.gotm.net/index.php?go=software&page=testcases, April 2007.

[87] A. S. Monin and A. M. Obukhov. Basic laws of turbulent mixing in the ground layer of the atmosphere. Trans. Geophys. Inst. Akad., 151:163{187, 1954.

[88] A. Morel. Optical modeling of the upper ocean in relation to its biogenous matter content (case I waters). J. Geophys. Res., 93:10749{10768, 1988.

[89] A. Morel and D. Antoine. Heating rate within the upper ocean in relation to its bio-optical state. J. Phys. Oceangr., 24:1652{1665, 1994.

[90] K. A. Moyer and R. A. Weller. Observations of surface forcing from the subduction experiment: A comparison with global model products and climatological datasets. J. Climate, 10:2725{2742, 1997.

[91] B. B. Nardelli, S. Marullo, and R. Santoleri. Diurnal variations in AVHRR SST elds: A strategy for removing warm layer e ects from daily images. Remote Sens. Environ., 95:47{56, 2005.

[92] I. M. Navon. Practical

[95] J. C. Ohlmann and D. A. Siegel. Ocean radiant heating. Part II: Parameterizing solar radiation transmission through the upper ocean. J. Phys. Oceanogr., 30:1849{1865, 2000.

[96] J. C. Ohlmann, D. A. Siegel, and C. D. Mobley. Ocean radiant heating. Part I:

[106] GODAE High Resolution Sea Surface Pilot Project. http://www.ghrsst-pp.org, April 2007.

[107] GODAE High Resolution Sea Surface Pilot Project. http://www.ghrsst-pp.org/sst-de nitions.html, April 2007.

[108] D. K. Ralston and M. T. Stacey. Shear and turbulence production across subtidal channels. J. Mar. Syst., 64:147{171, 2006.

[109] R. K. Reed. On estimating insolation over the o

[118] Y. Sasaki. Some basic formalisms in numerical variational analysis. Mon. Wea. Rev., 98:875{883, 1970.

[119] P. M. Saunders. The temperature at the ocean-air interface. J. Atmos. Sci., 24:269{273, 1967.

[120] M .E. Schiano. Insolatation over the western Mediterranean Sea: A comparison of direct measurement and Reed's formula. J. Geophys. Res., 101:3831{3838, 1996.

[121] A. Schiller and J. S. Godfrey. A diagnostic model of the diurnal cycle of sea surface temperature for use in coupled ocean-atmosphere models. J. Geophys. Res.,.

[130] R. C. Smith and K. S. Baker. Optical classi cation of natural waters. Limnol. Oceanogr., 23:260{267, 1978.

[131] J. Stark and C. Donlon. A new high-resolution operational sea surface temperature analysis for oceanography and meteorology. Eos Trans. AGU, Ocean Sci. Meet. Suppl., 87:Abstract OS12A{04, 2006.

[132] J. W. Stevenson and P. P. Niiler. Upper ocean heat budget during the Hawaii-to-Tahiti shuttle experiment. J. Phys. Oceanogr., 13:1894{1907, 1983.

[133] A. Stips, H. Burchard, K. Bolding, H. Prandke, and A. Wuest. Measurement and simulation of viscous dissipation rates in the wave a ected surface layer. Deep Sea Res. II, 52:1133{1155, 2005.

[134] H. Stommel. Observations of the diurnal thermocline. Deep Sea Res., 16:269{284, 1969.

[135] L. Stramma, P. Cornillon, R. A. Weller, J. F. Price, and M. G. Briscoe. Large diurnal sea surface temperature variability: Satellite and in situ measurements. J. Phys. Oceanogr., 56:345{358, 1986.

[136] A. C. Stuart-Menteth, I. S. Robinson, and P. G. Challenor. A global study of diurnal warming using satellite-derived sea surface temperature. J. Geophys. Res., 108:3155, 2003.

[137] A. C. Stuart-Menteth, I. S. Robinson, and C. J. Donlon. Sensitivity of

[140] Remote Sensing Systems. http://www.remss.com, April 2007.

[141] H. H. Syu and D. Neelin.

[152] P. J. Webster and R. Lukas. TOGA COARE: The Coupled Ocean - Atmosphere Response Experiment. Bull. Am. Meteorol. Soc., 73:1377{1416, 1992.

[153] L. Wei, Y. Rucong, L. Hailong, and Y. Yongqiang. Impacts of diurnal cycle of SST on intraseasonal variation of surface heat ux over the western Paci c warm pool. Adv. Atmos.

[143]